



저작자표시-비영리-변경금지 2.0 대한민국

이용자는 아래의 조건을 따르는 경우에 한하여 자유롭게

- 이 저작물을 복제, 배포, 전송, 전시, 공연 및 방송할 수 있습니다.

다음과 같은 조건을 따라야 합니다:



저작자표시. 귀하는 원저작자를 표시하여야 합니다.



비영리. 귀하는 이 저작물을 영리 목적으로 이용할 수 없습니다.



변경금지. 귀하는 이 저작물을 개작, 변형 또는 가공할 수 없습니다.

- 귀하는, 이 저작물의 재이용이나 배포의 경우, 이 저작물에 적용된 이용허락조건을 명확하게 나타내어야 합니다.
- 저작권자로부터 별도의 허가를 받으면 이러한 조건들은 적용되지 않습니다.

저작권법에 따른 이용자의 권리는 위의 내용에 의하여 영향을 받지 않습니다.

이것은 [이용허락규약\(Legal Code\)](#)을 이해하기 쉽게 요약한 것입니다.

[Disclaimer](#)

Fundamental Studies on Cassie equation and
Cassie-Baxter to Wenzel transition

Kwang Hui Jung

Department of Chemical Engineering

Graduate School of UNIST

Fundamental Studies on Cassie equation and Cassie-Baxter to Wenzel transition

A thesis/dissertation
submitted to the Graduate School of UNIST
in partial fulfillment of the
requirements for the degree of
Master of Science

Kwang Hui Jung

12.14.2018

Approved by



Advisor

Dong Woog Lee

Fundamental Studies on Cassie equation and Cassie-Baxter to Wenzel transition

Kwang Hui Jung

This certifies that the thesis/dissertation of Kwang Hui Jung is approved.

12.14.2018

signature



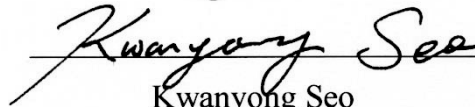
Advisor: Dong Woog Lee

signature



Sang Kyu Kwak

signature



Kwanyong Seo

Abstract

Wetting phenomena have been studied extensively due to their versatile applications such as self-cleaning, microfluidics, and anti-icing. The wettability can be evaluated by measuring contact angle and the contact angle can be predicted by several equations. For molecularly flat and chemically homogeneous surfaces, the Young's equation is used, and for a molecularly flat, chemically heterogeneous surface, the Cassie equation is used. Moreover, when the surfaces are rough, the Cassie-Baxter equation predicts the contact angle when the liquid droplet cannot penetrate rough pores on the surface, while the Wenzel equation is used for the case when the liquid droplet fully wets the surface. When intrinsic contact angles are lower than 90 degrees, the Wenzel state is thermodynamically favorable over the Cassie-Baxter state resulting in Cassie-Baxter to Wenzel transition over a certain period.

The Cassie equation has been successfully used for many decades, but its limitations are still being investigated through various experimental and theoretical studies. Also, fabrication of robust surfaces sustaining the Cassie-Baxter state without transitioning to the Wenzel state for prolonged periods is still a challenging task. Therefore, in this work, we systematically investigated the Cassie equation and Cassie-Baxter to Wenzel transition.

In Chapter 2, we measured water contact angles and analyzed droplet shapes to systematically investigate flat and chemically heterogeneous. A wide range of pattern sizes and spacings have been utilized to investigate the static contact angle changes due to chemical heterogeneity.

In Chapter 3, we fabricated a concave pillar inspired by the structure of leaf beetle pulvilli, which have hydrophobic concave hairy structures exhibiting self-cleaning property. Photolithography, anisotropic etching of silicon, and the Bosch process were utilized to make a robust hydrophobic surface.

Contents

Abstract	4
Contents	6
Lists of Figures	8
Lists of Tables	12
Chapter 1. Introduction	13
1.1 Previous studies of Wetting phenomena	13
1.2 Measurement of the Wettability	13
1.2.1 Goniometer	13
1.2.2 Capillary tube	14
1.2.3 Wilhelmy plate	15
1.2.4 Axisymmetric Drop Shape Analysis (ADSA)	16
1.3 Young's Equation	17
1.4 Other Equations	17
1.5 Contact Angle Hysteresis	19
Chapter 2. Revisiting Cassie equation	20
2.1 Experimental	20
2.2 Result and Discussion	23
2.3 Conclusion	35
2.4 CGMD Simulation	36
Chapter 3. Robust superhydrophobic surfaces via Concave pillar	39

3.1 Experimental	41
3.2 Result and Discussion	45
3.3 Conclusion	53
Chapter 4. Summary	54
Chapter 5. Reference	55
Chapter 6. Acknowledgments	61

List of Figures

Figure 1.1 Schematic of a goniometer. -----	14
Figure 1.2 Schematic of the cross section of a narrow capillary tube. -----	15
Figure 1.3 Schematic of the Wilhelmy plate method. -----	16
Figure 1.4 Schematic of a liquid droplet on a flat and homogeneous surface. -----	17
Figure 1.5 (a) Schematic of a liquid droplet on a flat and chemically heterogeneous surface. (b) the Wenzel state. (c) the Cassie-Baxter state. -----	18
Figure 2.1 (a) Schematic of the preparation of the smooth and chemically heterogeneous surface: (i) photolithography to make a hexagonal array circle pattern and (ii) FOTS silanization on the pattern. (b) Photograph of a deposited droplet on the smooth and chemically heterogeneous surface and inset is the patterned surface. Photograph of the patterned surface is observed before the photoresist is removed. Scale bar in the inset is 500 μm . -----	22
Figure 2.2 Cosine of the measured contact angles versus pattern diameter/distance between patterns, D/L , of (a) all samples, (b) samples with small pattern size ($D \leq 80 \mu\text{m}$) and (c) samples with large pattern size ($D \geq 160 \mu\text{m}$). Contact angles measured on samples with diameters less than 80 μm are represented by blue, and the contact angles measured on samples with diameters greater than 160 μm are represented by red. Each point is the averaged value of at least five different positions and the error bar indicates the standard deviation. Solid and dashed curves correspond to the Cassie equation and the Israelachvili-Gee model, ³² respectively. -----	26
Figure 2.3 Design of the photomask. D/L are 0.2 (a, b), and 0.6 (c, d), respectively, when pattern	

diameters are 1000 μm and 1500 μm . Each sample's size is 8 mm x 9 mm, and FOTS, which is represented by black, is deposited on silicon dioxide, which is represented by red. -----27

Figure 2.4. Cosine of the measured contact angles versus pattern diameter / distance between patterns, D/L , according to the distance between patterns. Solid curve corresponds to the Cassie equation. ----28

Figure 2.5. The absolute value of the averaged deviations between the experimental value and the Cassie equation for each diameter versus pattern diameter, D . Squares show the absolute value of the averaged deviation and the vertical lines on each plot indicate the standard deviation. The red solid line is a linear regression fit obtained by the least square method. The deviation and the standard deviation increase according to the increase in diameter. -----29

Figure 2.6. The absolute value of the averaged deviations between the experimental value and the Israelachvili-Gee model for each diameter versus pattern diameter, D . Squares show the absolute value of the averaged deviation and the vertical lines on each plot indicate the standard deviation. The continuous red line is obtained by the least square method. The deviation and the standard deviation increase according to the increase in diameter. -----29

Figure 2.7. Photograph of the water droplet on the chemically heterogeneous surfaces with D/L of 0.5 for 2 – 640 μm diameters (a-i) and 0.6 for 1000, 1500 μm diameters (j, k). Due to the transparency of the FOTS, water droplets and patterns were obtained separately, and then photographs were combined in the image software. -----31

Figure 2.8. Average of the absolute value of the deviation between the experimental value and the Cassie equation versus the ratio $\alpha = D/D_{DB}$ (pattern diameter/droplet base diameter). The continuous red line is obtained by a least square method except for the three points in the dashed circle. The deviation increases according to the ratio. -----32

Figure 2.9. Average of the absolute value of the deviation between the experimental value and the Israelachvili-Gee model versus the ratio $\alpha = D/D_{DB}$ (pattern diameter/droplet base diameter). The continuous red line is obtained by a least square method. The deviation increases according to the ratio. -----33

Figure 2.10. Obtaining the droplet base diameter on a chemically heterogeneous surface. -----34

Figure 2.11. Cosine of the contact angles using CGMD simulation (represented by black) and interaction energy, E_{int} (represented by blue) versus pattern diameter/distance between patterns, D/L at $D = 2$ nm. Dashed curve corresponds to the Cassie equation. This simulation result is obtained in collaboration with prof. Kwak's group. -----37

Figure 2.12. Water droplet morphology according to differing droplet positions. Initial model systems with D/L of 0.5 for $D = 16.2$ nm (which corresponds to $640 \mu\text{m}$ in the experimental system) depending on the initial position of the water droplets (a-c) and the water droplets after 100 ns (d-f). The final equilibrium contact angles are shown below. This simulation result is obtained in collaboration with prof. Kwak's group. -----38

Figure 3.1. (a) Schematic of potassium hydroxide (KOH) etching. KOH etches the silicon but the (111) plane is etched at a slower rate. (b) FE-SEM image of a concave after KOH and isopropyl alcohol (IPA) solution etching followed by nitric acid (HNO_3) and hydrogen fluoride (HF) solution etching. The scale bar is $10 \mu\text{m}$. -----41

Figure 3.2. (a-c) Photograph of the leaf beetle insect, and field emission scanning electron microscope (FE-SEM) image of a pulvilli of the leaf beetle with a concave structure. Scale bars are $20 \mu\text{m}$ and $10 \mu\text{m}$, respectively. (d) Schematic of the preparation of a concave pillar. (e) FE-SEM image of the concave pillar. The insets are a magnification of the concave pillar and a cross section of the concave pillar. Scale bars are $100 \mu\text{m}$ for the image, and $10 \mu\text{m}$ and $30 \mu\text{m}$ in the insets, respectively. -----44

Figure 3.3. FE-SEM images of concave pillar according to the etching conditions. The concave pillar etched with IPA 10% (a), 15% (b) and 20% for 10 minutes (c) and 20% for 15 minutes (d), respectively.

-----46

Figure 3.4. Measured contact angles versus pattern diameter/pitch between pillar centers, D/L , of the normal pillar (represented by red color) and the concave pillar (represented by blue color). Each point is the averaged value of at least five different positions and the error bars indicate the standard deviation. Red, blue, and black solid curves correspond to the Cassie-Baxter equation of normal pillar, concave pillar and when the intrinsic contact angle is 110° , respectively. Red and blue dashed curves correspond to the Wenzel equation of the normal pillar and concave pillar, respectively.

-----48

Figure 3.5. Underwater air injection test for the normal pillar (a), the concave pillar (b). The Cassie-Baxter state is maintained for the concave pillar during the air injection.

-----49

Figure 3.6. FE-SEM images of the normal pillar (a, b) and the concave pillar (c, d) used in Cassie-Baxter to Wenzel transition rate experiment.

-----50

Figure 3.7. (a) Schematic of the concave pillar and normal pillar with covered edges. (b) FE-SEM image of the normal pillar edge.

-----50

Figure 3.8. Cassie-Baxter to Wenzel transition rate of normal pillars and concave pillars. (a) Plot of fraction of Cassie-Baxter to Wenzel transition area versus time. (b) OM images of normal pillars and concave pillars immersed in water during the Cassie-Baxter to Wenzel transition rate experiment.

---52

List of Tables

Table 2.1 All samples used in measuring contact angles. -----	23
Table 3.1 Etching parameters of the Deep Si etcher. -----	42
Table 3.2 Diameters of the concave pillars. -----	45
Table 3.3 Intrinsic contact angles. -----	47

Chapter 1. Introduction

1.1 Previous studies of Wetting phenomena

Fabricating surfaces with a desired liquid wettability is an essential process in various industries, including self-cleaning,¹ water-repellent fabric,² medical devices,³ microfluidics,⁴⁻⁵ water/oil separation,⁶ ferroelectric insulators,⁷ anti-icing,⁸ gas evolution process,⁹⁻¹⁰ etc. The importance of wetting has been recognized for decades. Unexpected phenomena such as biofouling of ships, corrosion of pipes and bridges, and icing of airplanes lead to a huge cost loss. To prevent these phenomena, solid surfaces are artificially modified to have an appropriate wettability (hydrophobicity, hydrophilicity, oleophobicity, etc.).

Hence, it is essential to understand wetting phenomena in surface chemistry. Prior investigations of wetting phenomena presumably began in the 18th century. Laplace and Poisson investigated the fundamental studies of capillarity (which is closely related to wetting).¹¹⁻¹² Notably, Young developed the relationship between contact angles and interfacial tension when a liquid is deposited on a solid surface,¹³ and then Gibbs proved this concept thermodynamically.¹⁴ Since then, it has been recognized that liquid behavior on a surface is dominated by competition among the solid-vapor, solid-liquid, and liquid-vapor interfacial tensions. Complete wetting of the fluid on the solid surface takes place when the spreading coefficient (S_{slv}) is positive.¹⁵ The spreading coefficient is expressed by

$$S_{slv} = \gamma_{sv} - \gamma_{sl} - \gamma_{lv} \quad (1.1)$$

In contrast, the liquid has a sessile drop shape (partial wetting or dewetting) on the solid surface when the spreading coefficient is negative, and the contact angle of the sessile drop is determined from Young's equation (Section 1.3).¹⁶

1.2 Measurement of the Wettability

1.2.1 Goniometer

The wettability is measured by the contact angles of fluid. When measuring contact angles, the general technique is a direct measurement of the tangent angle from the sessile drop profile using a goniometer (Figure 1.1). The goniometer consists of a camera, a horizontal stage for placing substrates, a light source, and a syringe to deposit the droplet. Droplet volume is controlled by computer software, and then the liquid droplet hanging from the syringe is gently deposited on the substrate. Next, the droplet

image is captured by the camera, and the droplet profile image is analyzed in the software. This method is the most convenient method and has the advantage that contact angles can be measured even with small liquid droplets and substrates.

However, the goniometer method results can be affected by contamination due to its size and be dependent on the droplet size since external forces such as gravity affect the droplet shape,¹⁷ so it has approximately a $\pm 2^\circ$ error. Also, an enclosed cell is required to prevent contamination from the air and evaporation when measuring the contact angle of volatile liquids.

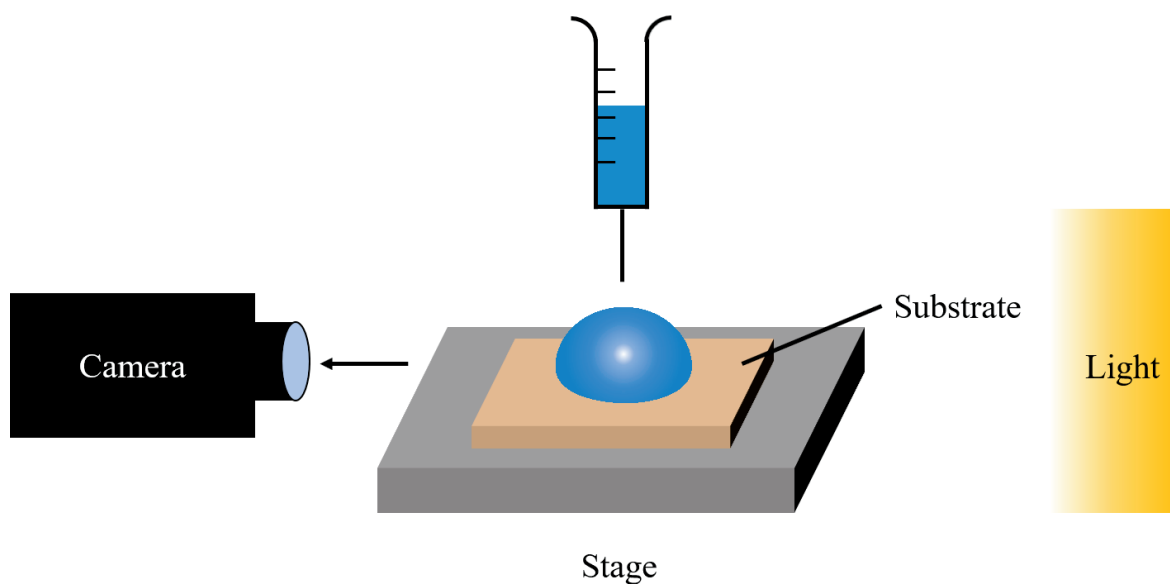


Figure 1.1. Schematic of a goniometer.

1.2.2 Capillary tube

In a narrow capillary tube of circular cross section, the meniscus forms at the interface between two fluids (usually liquid, air) and consists of a sphere like surface having radius R (Figure 1.2). Capillary height h is expressed by

$$h = \frac{2\gamma_{lv} \cos \theta}{\rho g a} \quad (1.2)$$

where γ_{lv} , ρ , g , and a are the surface tension of the liquid, the density of the fluid, the gravitational acceleration, and the radius of tube, respectively. The contact angle can be obtained by measuring h and

a. This equation is acquired from the Young-Laplace equation, and it is known as the Jurin rule or Jurin height after James Jurin developed this effect in 1718.¹⁸⁻¹⁹

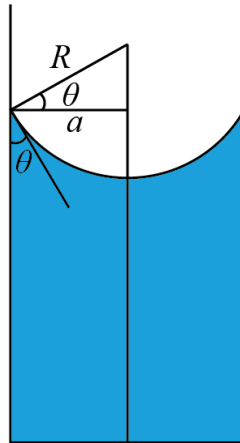


Figure 1.2. Schematic of the cross section of a narrow capillary tube.

1.2.3 Wilhelmy plate

The Wilhelmy plate is used to measure the interfacial tension at a vapor-liquid (or liquid-liquid) interface.²⁰ When a thin, flat plate (filter paper, glass or platinum) is immersed into a liquid vertically, the shift in weight and force due to the wetting and buoyancy are measured by a tensiometer or microbalance. The force F is represented by the Wilhelmy equation and expressed by

$$F = \gamma_{lv}l \cos \theta - V\Delta\rho g \quad (1.3)$$

where γ_{lv} and l are the surface tension of the liquid and the length of the contact line which is perimeter of the plate ($2w + 2d$), w and d are the plate width and thickness, respectively, θ is the contact angle, V is the volume of the liquid, $\Delta\rho$ is the density difference between air and liquid, and g is the gravitational acceleration (Figure 1.3). Therefore, the contact angles can be easily obtained from the liquid surface tension and the perimeter of the plate. This method has the advantage that it can measure the contact angle of rods or fibers, which is hard to measure with the conventional method.

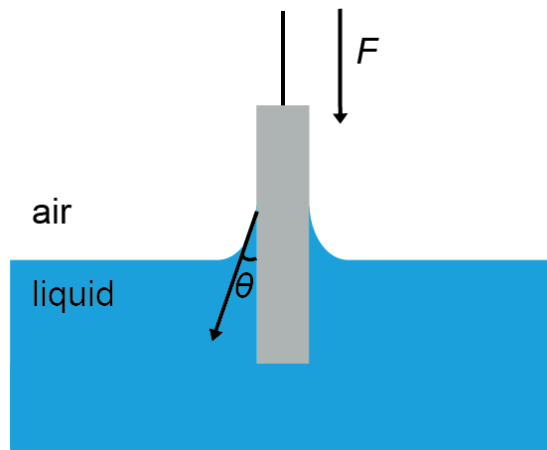


Figure 1.3. Schematic of the Wilhelmy plate method.

1.2.4 Axisymmetric Drop Shape Analysis (ADSA)

There are a lot of methods to figure out the surface tension of liquid and contact angles from a deposited droplet and a captive bubble, but the deposited droplet deforms due to gravitational forces. Surface tension causes a droplet to be spherical, but gravitational forces flatten the droplet profile. This relationship between the surface tension and gravitational forces are represented in the Laplace equation, which provides the feasibility of obtaining the surface tension by investigating the droplet shape. Firstly, Bashforth and Adams investigated the droplet shape by using the Laplace equation,²¹ and since then, many studies have been developed.²²⁻²³

The development of computers helped improve the drop profile analysis. The axisymmetric drop shape analysis (ADSA) has been studied since it was established by Rotenberg et al.^{24, 25-26} This method has a reproducibility of $\pm 0.2^\circ$ and is considered to be the most accurate technique to measure the contact angle. The main principle of this method is to match the experimental droplet profile to the most suitable theoretical profile. There are two fundamental assumptions.²⁷

- (i) The droplet is Laplacian and axisymmetric.
- (ii) The only external force is gravity.

The algorithm finds the surface tension that forms the theoretical shape which best corresponds the droplet shape.

1.3 Young's Equation

When a liquid droplet is deposited on a flat and homogeneous surface (Figure 1.4), it has a spherical shape due to interfacial tension of liquid and vapor. The contact angle is established at the liquid-solid-vapor intersection, which is called the “three phase contact line (TCL).” On hydrophilic surfaces, water droplets have low contact angles, and water droplets have high contact angles on hydrophobic surfaces. This contact angle is predicted by Young's Equation¹³ and expressed by

$$\cos \theta_{Young} = \frac{\gamma_{sv} - \gamma_{sl}}{\gamma_{lv}} \quad (1.4)$$

where γ_{sv} , γ_{sl} , and γ_{lv} are the interfacial tensions of solid-vapor, solid-liquid, and liquid-vapor, respectively. Young's equation is used to roughly predict how the liquid will wet the surface, but this equation can only predict contact angles on ideal surfaces (smooth, homogenous, rigid, and inert surfaces). However, in real life situations, substrates generally have physical roughness and chemical heterogeneities, so other equations have been developed.

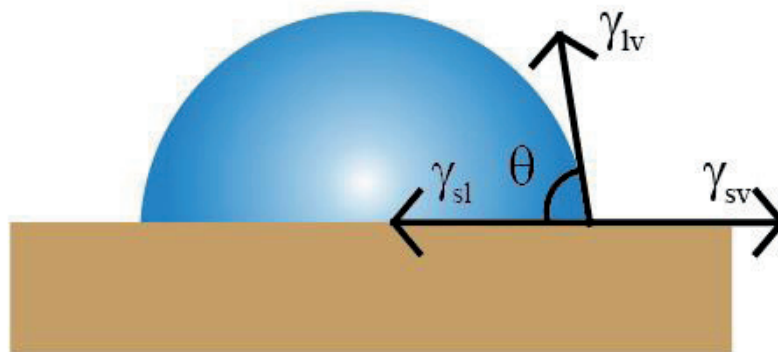


Figure 1.4. Schematic of a liquid droplet on a flat and homogeneous surface.

1.4 Other Equations

Real surfaces have physical roughness and chemical heterogeneities. When a surface is flat and chemically heterogeneous, the contact angle can be predicted by the Cassie equation²⁸ (Figure 1.2a). The Cassie equation is expressed by

$$\cos \theta_{Cassie} = f_1 \cos \theta_1 + f_2 \cos \theta_2 \quad (1.5)$$

where f_1, f_2 and θ_1, θ_2 are the area fractions and intrinsic contact angles of each material, respectively, and $f_1 + f_2 = 1$.

In other cases, when surfaces have physical roughness, there are two states. First, the liquid wets the surface entirely so there is only the solid-liquid interface under the liquid droplet (Figure 1.2b). In this state, the Wenzel equation²⁹ is used to predict contact angles, and it is expressed by

$$\cos \theta_{wenzel} = r \cos \theta \quad (1.6)$$

where r and θ are the roughness factor, which is the ratio of the real area of the solid to the projected area, and intrinsic contact angle, respectively. In the Wenzel state, liquid droplets generally have low mobility, so the droplets are pinned on the surface.

Second, air is trapped under the liquid droplet, so solid-vapor, solid-liquid, and liquid-vapor interfaces exist under the droplet. In this case, the Cassie-Baxter equation³⁰ is used to calculate the contact angle, and it is expressed by

$$\cos \theta_{Cassie-Baxter} = f \cos \theta + f - 1 \quad (1.7)$$

where f and θ are the area fraction and intrinsic contact angle of the solid, respectively. This equation is similar with the Cassie equation, but the second material is air. In the Cassie-Baxter state, liquid droplets generally have large contact angles and high mobility.

In addition, there are many other equations. for example, modified Cassie equations which consider line tension,³¹ molecular-sized patches,³² and other factors.³³⁻³⁷ Additionally, modified Wenzel equations have also been developed.³⁸⁻³⁹ However, the above three equations are widely used to predict contact angles due to their ease of application.



Figure 1.5. (a) Schematic of a liquid droplet on a flat and chemically heterogeneous surface. (b) the Wenzel state. (c) the Cassie-Baxter state.

1.5 Contact Angle Hysteresis

In real situations, there are many contact angles in metastable states, so static contact angles are not sufficiently enough to describe wetting phenomena. The contact angle hysteresis is obtained from dynamic contact angles. When the liquid droplet expands, the TCL advances forward, and dynamic contact angles are formed, and this dynamic contact angle is called the advancing contact angle, θ_a . Conversely, when the liquid droplet is withdrawn, the TCL recedes back, and this dynamic contact angle is called the receding contact angle, θ_r . On the other hand, when the droplet is sliding, the forward angle refers to the advancing contact angle and the rear angle refers to the receding contact angle. An advancing contact angle has the maximum contact angle while a receding contact angle has the minimum contact angle, and the contact angle hysteresis is defined as the difference between advancing angles and receding angles.

The contact angle hysteresis has been studied recently.⁴⁰⁻⁴¹ If a surface is an ideal solid surface which is a smooth, homogeneous, rigid, and inert surface, there is no contact angle hysteresis. However, if physical roughness or chemical heterogeneity exist, then the surface has an energy barrier on the hydrophobic patch or the air layer caused by roughness.⁴² This energy barrier pins the TCL, so when advancing, it leads to an increment of the dynamic contact angle. Conversely, when receding, it leads to a decrease of the dynamic contact angle.

Chapter 2. Revisiting Cassie equation

The Cassie equation is the most widely used equation which predicts the contact angle on the chemically heterogeneous, flat, and smooth surfaces. However, Gao and McCarthy raised the question about the validity of the Cassie equation by using Extrand's experiment.⁴³⁻⁴⁴ They demonstrated that the contact angle is not affected by the three-phase contact area (TCA) instead of three-phase contact line (TCL). Since then, modified Cassie equations which include the TCL fraction have been developed and various follow up studies showed the importance of the contact line.^{34, 37, 45-48}

However, it is difficult to obtain the line fraction experimentally, so researchers generally applied the Cassie equation to calculate the contact angles of chemically heterogeneous and flat surfaces because it is accurate when the heterogeneity size is sufficiently smaller than the water droplet size.⁴⁹⁻⁵¹ Although the Cassie equation is still being used, it is crucial to know that there are two conditions that need to be met for the Cassie equation to be applied.

- (i) the droplet size is sufficiently larger than the heterogeneous patch size.
- (ii) heterogeneous patches are uniformly distributed.

There are several studies regarding the first condition that are investigated by using simulations having nano-scale heterogeneities.⁵²⁻⁵⁶ In experimental results, although nano-scale heterogeneities are sufficiently smaller than the droplet size, there are discrepancies between the Cassie contact angles and measured contact angles due to the hydrophobic effect.⁵⁷ Therefore, it is crucial to investigate the heterogeneous surface having micron-scale heterogeneities and to compare with heterogeneous surface with nano-scale heterogeneities. In this work, the heterogeneous surface is investigated systematically by obtaining both experimental results (micron-scale) and simulation results (nano-scale) to fully understand the applicability of the Cassie equation in real situations.

2.1 Experimental

Preparation of chemically heterogeneous surfaces. Figure 2.1a represents a schematic of the preparation of chemically heterogeneous surfaces. A 4-inch silicon wafer (P-type, 100) was thermally oxidized to a thickness of 1.69 μm in the furnace (KHD-306, KSM). The wafer was immersed in a 3:1 sulfuric acid to 30% hydrogen peroxide solution for 30 min at 80 $^{\circ}\text{C}$. Following this, it was rinsed with deionized (DI) water and dried using a nitrogen gun. Photoresist (AZ5214E) was spin coated on the

silicon dioxide, and the photoresist was baked, exposed by ultraviolet (UV) light (MA/BA6-8, Suss Microtec), and developed (AZ 300 MIF Developer), so a hexagonal array circle pattern was made. Trichloro-(1H, 1H, 2H, 2H-perfluorooctyl) silane (FOTS), which has about a 100-degree contact angle was deposited by a SAM coater (AVC – 150, SORONA) from the vapor phase, and then the photoresist was removed by using acetone. Following this, it was rinsed with DI water and dried using a nitrogen gun. Therefore, the circle was FOTS and the rest of the surface was silicon dioxide. A lot of samples ranging from 2 to 1500 μm in diameter D and from 4 to 7500 μm in center-to-center spacing L between circle patterns were made (Figure 2.1b).

Contact angle measurement. Figure 2.1b represents a photograph of a water droplet deposited on the chemically heterogeneous surface. The water contact angle of fabricated samples was measured by using a goniometer (Phoenix 300, SEO) in at least five different positions per sample for statistical analysis. DI water droplets with a volume of 6 μL hanging from the syringe were gently deposited on the samples. Contact angles were measured parallel to the rows because contact angles differ according to the viewing angle.⁵⁸ The water droplets deformed significantly on the samples with large diameter, so we measured contact angles by averaging the left and right contact angles.

Atomic Force Microscopy (AFM). AFM (MultiMode V, Veeco) was used to confirm the uniformity of silicon dioxide and the height of the FOTS layer.

Optical microscopy (OM). An optical microscope (Axio Scope A1, ZEISS) was used to observe the hexagonal array patterns. Since the FOTS is transparent, patterns were observed before the removal of the photoresist, and the images of the patterns are overlapped with droplet images by using an image software.

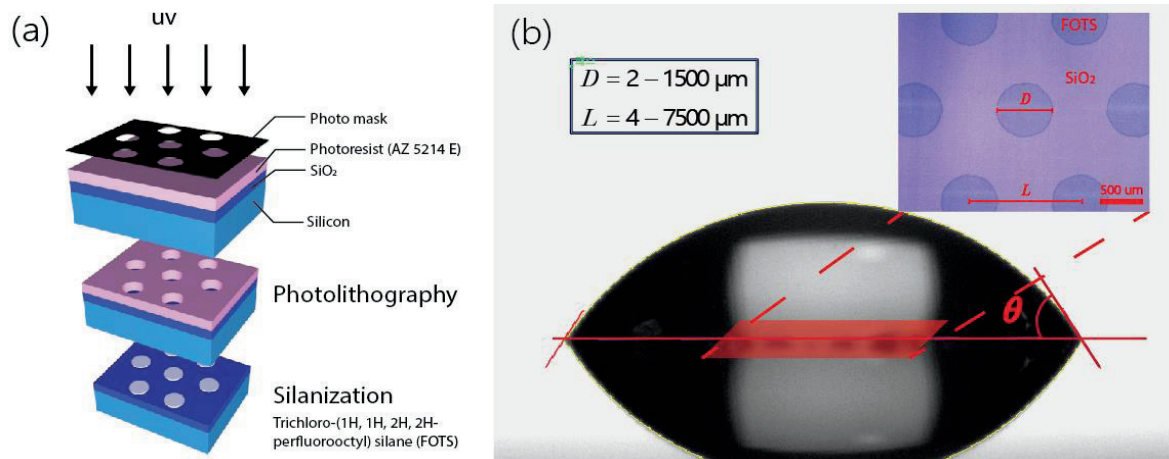


Figure 2.1. (a) Schematic of the preparation of the smooth and chemically heterogeneous surface: (i) photolithography to make a hexagonal array circle pattern and (ii) FOTS silanization on the pattern. (b) Photograph of a deposited droplet on the smooth and chemically heterogeneous surface and inset is the patterned surface. Photograph of the patterned surface is observed before the photoresist is removed. Scale bar in the inset is 500 μm .

2.2 Result and Discussion

To confirm the flat, smooth, and chemically heterogeneous surface, we measured the root-mean-square roughness using AFM. The root-mean-square roughness of the silicon dioxide and the FOTS layer are 0.296 nm, 2.13 nm, respectively, and the height of the FOTS is ~ 15 nm. Hence, the roughness effect on the apparent contact angle is negligible since the pattern height is sufficiently small compared to the lateral dimension ($\geq 2 \mu\text{m}$) of the patterns.

Patterned surfaces with various pattern sizes ($D = 2 - 1500 \mu\text{m}$) and center-to-center spacings ($L = 4 - 7500 \mu\text{m}$) (Figure 1b) were fabricated to systematically investigate the effects of D and L on the static contact angles. A total of 67 samples were made (Table 2.1) and all contact angles were measured in a parallel direction, which is because the apparent contact angles can vary depending on the viewing angles⁵⁸ or when pattern sizes are large.

Table 2.1. All samples used in measuring contact angles.

Sample number	$D, \mu\text{m}$	$L, \mu\text{m}$	$f(\text{FOTS})$	D/L
1	2	4	0.227	0.500
2	2	6	0.101	0.333
3	2	8	0.057	0.250
4	2	12	0.025	0.167
5	2	16	0.014	0.125
6	2	24	0.006	0.083
7	6	12	0.227	0.500
8	6	18	0.101	0.333
9	6	24	0.057	0.250
10	6	36	0.025	0.167
11	6	48	0.014	0.125
12	6	72	0.006	0.083
13	10	20	0.227	0.500
14	10	30	0.101	0.333
15	10	40	0.057	0.250
16	10	60	0.025	0.167
17	10	80	0.014	0.125

18	10	120	0.006	0.083
19	20	40	0.227	0.500
20	20	60	0.101	0.333
21	20	80	0.057	0.250
22	20	120	0.025	0.167
23	20	160	0.014	0.125
24	20	240	0.006	0.083
25	40	42	0.823	0.952
26	40	49	0.604	0.816
27	40	60	0.403	0.667
28	40	75	0.258	0.533
29	40	80	0.227	0.500
30	40	120	0.101	0.333
31	40	160	0.057	0.250
32	80	84	0.823	0.952
33	80	98	0.604	0.816
34	80	120	0.403	0.667
35	80	150	0.258	0.533
36	80	160	0.227	0.500
37	80	240	0.101	0.333
38	80	320	0.057	0.250
39	160	170	0.803	0.941
40	160	196	0.604	0.816
41	160	240	0.403	0.667
42	160	320	0.227	0.500
43	160	480	0.101	0.333
44	160	640	0.057	0.250
45	160	1280	0.014	0.125
46	320	340	0.803	0.941
47	320	392	0.604	0.816
48	320	480	0.403	0.667
49	320	640	0.227	0.500
50	320	960	0.101	0.333
51	320	1280	0.057	0.250

52	320	2560	0.014	0.125
53	640	680	0.803	0.941
54	640	784	0.604	0.816
55	640	960	0.403	0.667
56	640	1280	0.227	0.500
57	640	1920	0.101	0.333
58	640	2560	0.057	0.250
59	640	5120	0.014	0.125
60	1000	1250	0.580	0.800
61	1000	1667	0.326	0.600
62	1000	2500	0.145	0.400
63	1000	5000	0.036	0.200
64	1500	1875	0.580	0.800
65	1500	2500	0.326	0.600
66	1500	3750	0.145	0.400
67	1500	7500	0.036	0.200

Figure 2.2 shows the cosine of measured contact angles corresponding to the ratio between the pattern diameter and distance between patterns, D/L . The solid line and dashed line indicate Cassie equation and Israelachvili-Gee model,³² respectively. The measured Young contact angles of the FOTS and the silicon dioxide are 99.0° and 40.2° , respectively.

As the diameter of the pattern increases, the difference between the experimental contact angle and the Cassie angle also increases. When $D \leq 80 \mu\text{m}$, the measured contact angles are consistent with angles obtained from the Cassie equation. Moreover, the standard deviation of the measured contact angles is small, indicating that (i) apparent contact angles are barely affected by the position where the droplet is placed, and (ii) droplets are axisymmetric. Conversely, when $D \geq 160 \mu\text{m}$, deviation between the Cassie angle and the measured angle is relatively high. Also, a larger standard deviation of apparent contact angles is measured compared to that of samples where $D \leq 80 \mu\text{m}$.

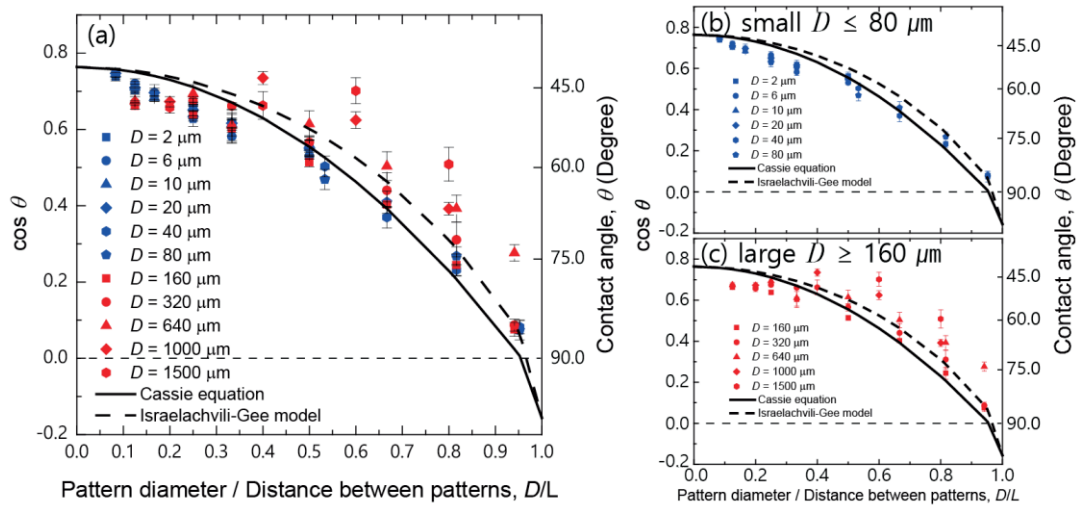


Figure 2.2. Cosine of the measured contact angles versus pattern diameter/distance between patterns, D/L , of (a) all samples, (b) samples with small pattern size ($D \leq 80 \mu\text{m}$) and (c) samples with large pattern size ($D \geq 160 \mu\text{m}$). Contact angles measured on samples with diameters less than $80 \mu\text{m}$ are represented by blue, and the contact angles measured on samples with diameters greater than $160 \mu\text{m}$ are represented by red. Each point is the averaged value of at least five different positions and the error bar indicates the standard deviation. Solid and dashed curves correspond to the Cassie equation and the Israelachvili-Gee model,³² respectively.

Another important point to note is that large D/L values result in large deviations from the Cassie equation but for small D/L , the measured contact angles are relatively consistent with the Cassie angles even in the case of large pattern diameters. The spacing between the pattern centers (L) is large compared with the water droplet size when the diameter of the pattern is large, so most of the droplet can be located, due to the size of the sample, at a portion where there is little hydrophobic region according to the position of the deposition. Figure 2.3a, b shows that for samples where the pattern size is 1000 or 1500 μm , when D/L is 0.2, the spacing between the patterns is large (5 mm – 7.5 mm, table 2.1) and the hydrophobic portion is small, due to the sample size, and spacing is large compared to the water droplet size ($\sim 3.7 \text{ mm}$, figure 2.7). Therefore, most water droplets could be deposited on silicon dioxide surfaces with almost no FOTS patterns. In contrast, with large D/L (Figure 2.3c-d), there are many hydrophobic patterns, and these patterns affect the water droplet base line. Hence, the water droplet is considerably deformed (figure 2.7) by the pinning effect of the hydrophobic patterns, so measured contact angles have large deviations from the Cassie equation and large standard deviations

according to the deposited positions. Figure 2.4 shows that when the spacings are larger than the droplet size (represented by red triangles), there are small discrepancies between the measured contact angles and the Cassie angles, but when the spacings are smaller than the droplet size, water droplet base lines are affected by hydrophobic patterns and deformed, so discrepancies and standard deviations become larger in the case of large pattern diameters.

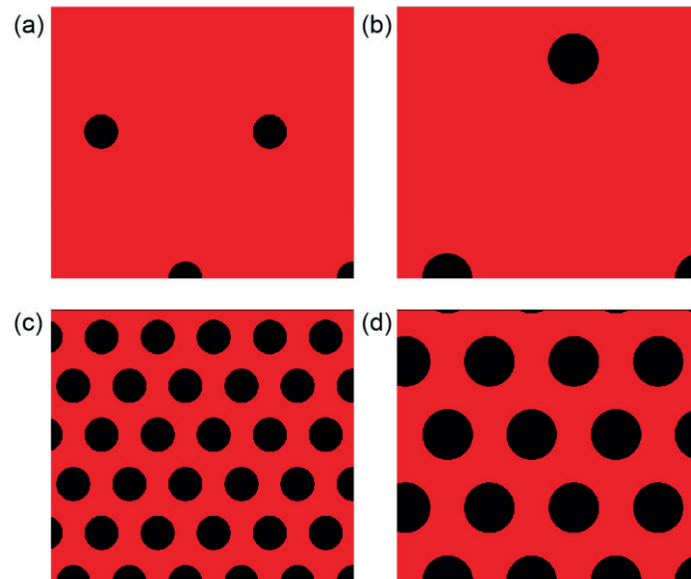


Figure 2.3. Design of the photomask. D/L are 0.2 (a, b), and 0.6 (c, d), respectively, when pattern diameters are 1000 μm and 1500 μm . Each sample's size is 8 mm x 9 mm, and FOTS, which is represented by black, is deposited on silicon dioxide, which is represented by red.

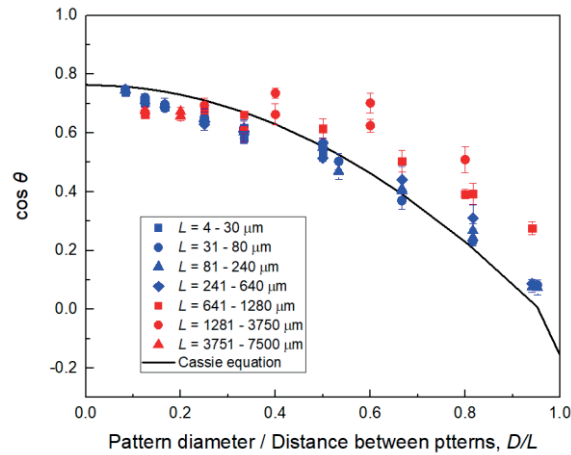


Figure 2.4. Cosine of the measured contact angles versus pattern diameter / distance between patterns, D/L , according to the distance between patterns. Solid curve corresponds to the Cassie equation.

To investigate the discrepancies between the measured contact angle and the Cassie equation in more detail, the absolute value of the averaged differences between the cosine values of measured contact angles and Cassie angles, $\Delta\cos\theta = |\cos\theta_{CA} - \cos\theta|$, are plotted against the diameter of the pattern (Figure 2.5, plot of the deviations from the Israelachvili-Gee model³² is in Figure 2.6). The plot shows that the $\Delta\cos\theta$ increases as the pattern diameter increases. Also, the standard deviation of $\Delta\cos\theta$ tends to increase according to the increment of the diameter, which is shown by larger error bars at large D values.

When the diameter of the pattern is smaller than 320 μm (represented by blue), deviations from the Cassie equation and standard deviation are small. However, when the diameter of the pattern is larger than 640 μm (represented by red), discrepancies from the Cassie equation and standard deviations are much larger compared to that of $D \leq 320 \mu\text{m}$. The large values of $\Delta\cos\theta$ and the standard deviation indicates that the measured contact angles highly depend on the position where water is deposited even for the same samples, which result in the deformation of the shape of water droplets. Indeed, the droplets deposited on the patterns having $D \geq 640 \mu\text{m}$ show non-circular shapes (Figure 2.7i), which seemed to be deformed along the circular patterns. Therefore, it is obvious that predicting the contact angle with the Cassie equation is difficult, as the pattern diameter is larger than 640 μm when 6 μL of water droplet is used (which approximately has $D_{DB} = 3.87 \text{ mm}$, when the contact angle is $\sim 52.0^\circ$).

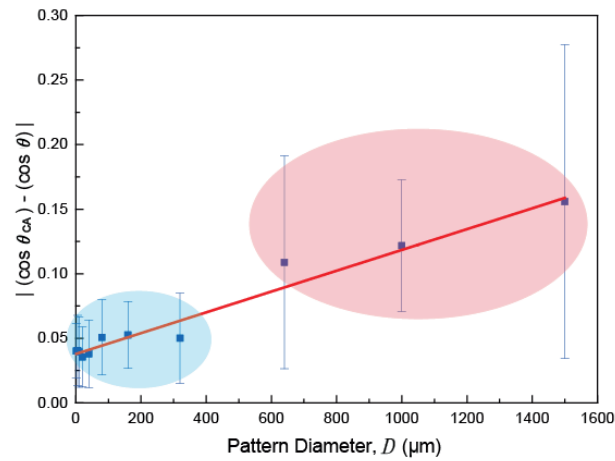


Figure 2.5. The absolute value of the averaged deviations between the experimental value and the Cassie equation for each diameter versus pattern diameter, D . Squares show the absolute value of the averaged deviation and the vertical lines on each plot indicate the standard deviation. The red solid line is a linear regression fit obtained by the least square method. The deviation and the standard deviation increase according to the increase in diameter.

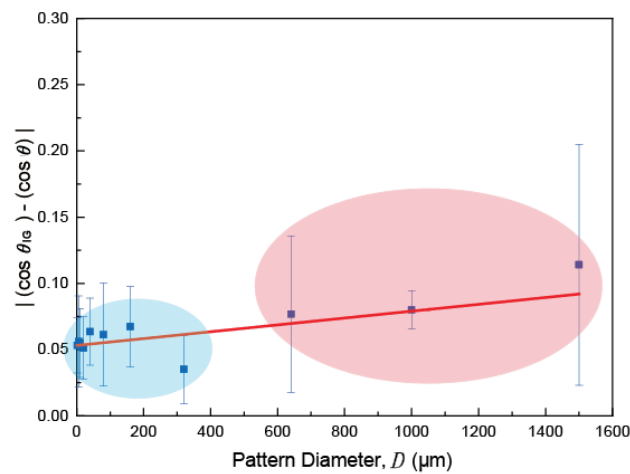


Figure 2.6. The absolute value of the averaged deviations between the experimental value and the Israelachvili-Gee model for each diameter versus pattern diameter, D . Squares show the absolute value of the averaged deviation and the vertical lines on each plot indicate the standard deviation. The continuous red line is obtained by the least square method. The deviation and the standard deviation increase according to the increase in diameter.

Figure 2.7 shows the shape of the water droplets as a function of pattern diameter. Droplets, deposited on the substrate with D/L of 0.5 for $D = 2 - 640 \mu\text{m}$ and 0.6 for $D = 1000, 1500 \mu\text{m}$, were observed with the optical microscope for each diameter. Images show the relationship between the degree of deformation and the deviation from the Cassie equation, and the deformation of the TCL of the droplet along the hydrophobic patterns by the pinning effect.⁴² When the diameter of the pattern is smaller than $320 \mu\text{m}$, there are some distortions, but the droplet has a nearly circular shape (Figure 2.7a-h). However, when the diameter of the pattern is greater than $640 \mu\text{m}$, the shape of the droplet completely deviates from the shape of a circle (Figure 2.7i-k). It results in a large deviation from the Cassie equation and large standard deviations due to various shapes (Figure 2.5). Therefore, when the droplet shape deviates greatly from the circle, it is difficult to predict the contact angle by using the Cassie equation.

The ability to deposit water droplets having a specific shape is advantageous for printing applications, including ink-jet printing⁵⁹ and liquid metal printing.⁶⁰ This work presents the ratio between droplet volumes and pattern size to show a hexagonal shape droplet in a heterogeneous and flat surface. The droplet shape is distorted to become more hexagonal when the pattern diameter is $40 \mu\text{m}$ (Figure 2.7e), and when the pattern diameter is $80 \mu\text{m}$ (Figure 2.7f), the droplet shape becomes a hexagonal. The hydrophobic pattern with hexagonal array has a sixfold symmetry energy barrier in the rows, and this energy barrier prevents the contact line from advancing any further. Consequently, when the pattern diameter is $80 \mu\text{m}$, the energy barriers of the rows are greater than the surface tension of the droplet, and this results in a hexagonal shape.⁶¹ However, when the pattern diameter becomes greater than $80 \mu\text{m}$, the energy barrier of each individual pattern, not rows, becomes large enough to prevent the contact line from advancing. As a result, the droplet loses the hexagonal shape, but maintains a shape resembling a circle. Therefore, when the $6 \mu\text{L}$ water droplet is deposited on the hexagonal array heterogeneous surface having $80 \mu\text{m}$ pattern diameter, water droplets have a hexagonal shape regardless of where they are deposited.

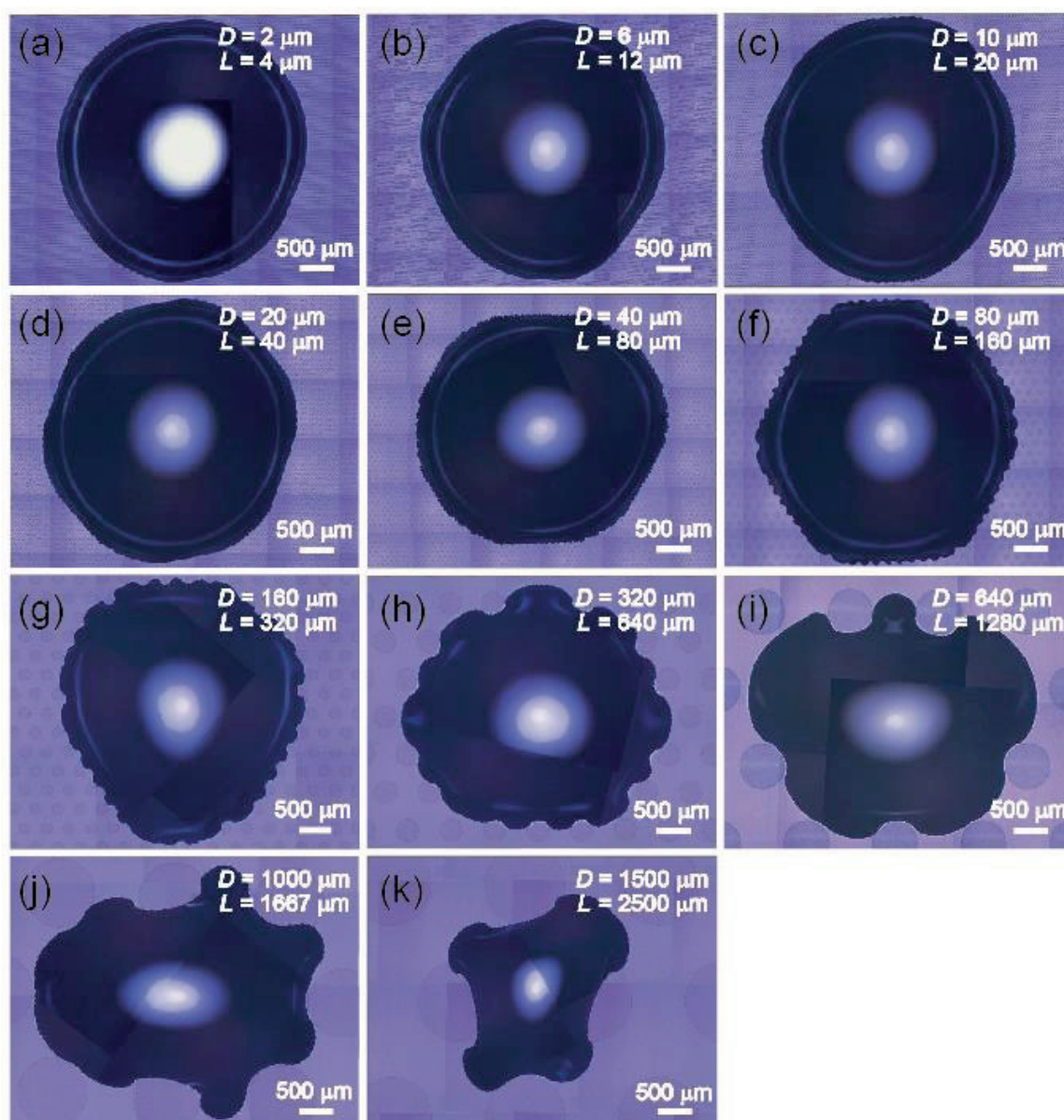


Figure 2.7. Photograph of the water droplet on the chemically heterogeneous surfaces with D/L of 0.5 for 2 – 640 μm diameters (a-i) and 0.6 for 1000, 1500 μm diameters (j, k). Due to the transparency of the FOTS, water droplets and patterns were obtained separately, and then photographs were combined in the image software.

Previous papers compared the size of the heterogeneity with droplet volume or droplet base diameter before deposition.^{52-53, 56, 62} However, it is significant to know the correlation between the heterogeneity size and base diameter after deposition because even with the same volume, they have different diameters depending on the interfacial tension of the substrate.

Figure 2.8 shows the absolute values of deviations in all samples versus the ratio of the pattern diameter D to the droplet base diameter D_{DB} , $\alpha = D/D_{DB}$ (plot of the deviations from Israelachvili-Gee model³² is in Figure 2.9). The deviation increases as α increases but there are some outliers which are indicated by dashed line circle. The reason for this is the same as that described above. Due to the sample size, the heterogeneous surfaces behave like homogeneous surfaces since there is large spacing between patterns, L . Some of the droplets can be placed only on a silicon dioxide surface while other droplets are placed over surfaces containing both silicon dioxide and FOTS. Therefore, there are large standard deviations in patterns with large diameter (Figure 2.5), and it is difficult to predict the contact angle with the Cassie equation, even if these outliers show small difference values. It seems that the critical ratio $\alpha_{critical}$ is ~ 0.17 . When the ratio α becomes larger than ~ 0.67 , experimentally measured contact angles don't give a good agreement with the Cassie equation with the exception of outliers.

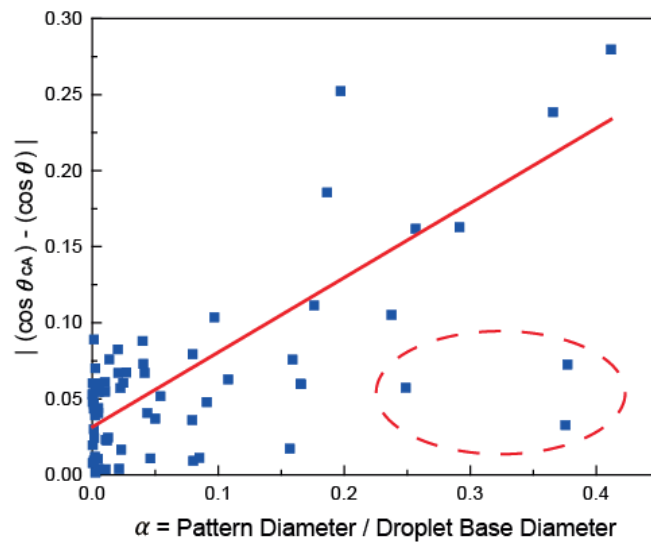


Figure 2.8. Average of the absolute value of the deviation between the experimental value and the Cassie equation versus the ratio $\alpha = D/D_{DB}$ (pattern diameter/droplet base diameter). The continuous red line is obtained by a least square method except for the three points in the dashed circle. The deviation increases according to the ratio.

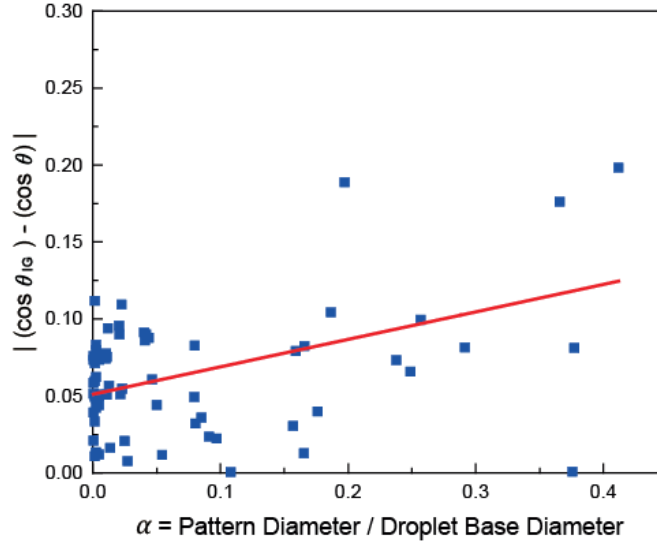


Figure 2.9. Average of the absolute value of the deviation between the experimental value and the Israelachvili-Gee model versus the ratio $\alpha = D/D_{DB}$ (pattern diameter/droplet base diameter). The continuous red line is obtained by a least square method. The deviation increases according to the ratio.

Before obtaining the droplet base diameter, D_{DB} , we assumed that (i) gravitational forces can be neglected and (ii) all droplets are considered truncated spheres. Based on simple geometry analysis, the volume of a truncated sphere is expressed by

$$V = \frac{1}{3}\pi r^3 (2 + \cos \theta)(1 - \cos \theta)^2 \quad (2.1)$$

where V is the volume of the truncated sphere, r is the radius of the truncated sphere, and θ is the measured contact angle. The radius of the truncated sphere is given by:

$$D_{DB} = r \sin \theta \quad (2.2)$$

$$r = \frac{D_{DB}}{\sin \theta} \quad (2.3)$$

When equation (7) and (9) are combined,

$$V = \frac{1}{3}\pi \left(\frac{D_{DB}}{\sin \theta}\right)^3 (2 + \cos \theta)(1 - \cos \theta)^2 \quad (2.4)$$

$$D_{DB} = \sin \theta \sqrt[3]{\frac{3V}{\pi (2 + \cos \theta)(1 - \cos \theta)^2}} \quad (2.5)$$

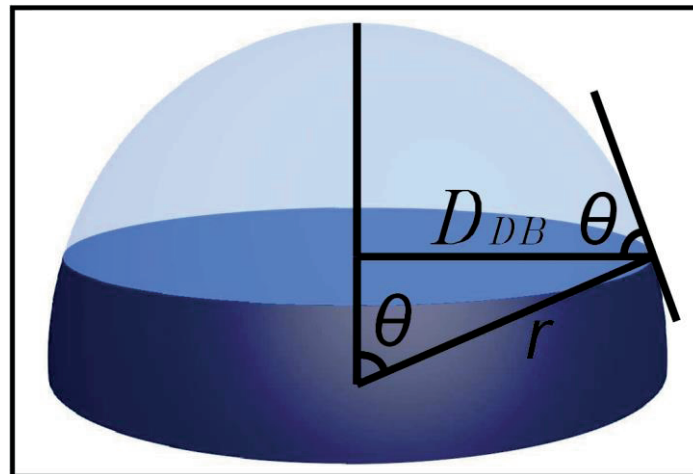


Figure 2.10. Obtaining the droplet base diameter on a chemically heterogeneous surface.

2.3 Conclusion

In chapter 2, we measured static water contact angles on smooth and chemically heterogeneous surfaces and these surfaces are systematically investigated. The deviation, between the measured contact angles and the Cassie equation, and the standard deviations increase with the increase of pattern diameter. When pattern diameter is greater than 640 μm , the measured contact angles largely deviate from the Cassie equation. With a diameter of 640 μm , the energy barrier of an individual hydrophobic pattern is larger than the surface tension. Hence, droplet shapes have a large deviation from a circular shape and it is obvious that predicting the contact angle with the Cassie equation is difficult, as the pattern diameter is larger than 640 μm when a 6 μL water droplet is used. Moreover, at the ratio between water droplet volume and pattern size ($V = 6 \mu\text{L}$, $D = 80 \mu\text{m}$), droplets have a hexagonal shape due to the energy barrier of the hydrophobic pattern with a hexagonal array and it is advantageous for printing application. Also, when the ratio between the diameter of the water droplet base and the pattern diameter is greater than ~ 0.17 , the Cassie equation is no longer valid.

This work provides a better understanding for the fundamental wetting behavior of liquids on the smooth, flat and chemically heterogeneous surfaces, and criteria in which the Cassie equation can predict contact angles. However, it requires additional analysis that contact angles are compared with the modified Cassie equation that includes line fractions, instead of area fractions, by using the simulation.

2.4 CGMD simulation

Coarse- Grained molecular dynamics (in collaboration with professor Sang Kyu Kwak's groups).

FOTS pattern on SiO₂ layer was modeled with pattern diameter 2.0 and 16.2 nm, which were correspond to 80 and 640 μm of experimental systems, respectively. For diameter of 2.4 nm model, 12 models were constructed with changing the ratio of diameter of the pattern D to pattern spacing L from $D/L = 0.083$ to 0.5.

Pattern with diameter 16.2 nm model was modeled when D/L is 0.5 and contact angle was measured with changing initial position of water droplet on surface. SiO₂ layers were kept constraint and periodic boundary condition was applied in x and y directions, and the thickness of SiO₂ layer was set to 2 nm to prevent self-interaction of water across the layer. Droplet diameter was set to 60 nm and the x and y length of SiO₂ layer are established to three times of droplet size, and system size was constructed 1800×1800×1200 nm³.

Water, FOTS, and SiO₂ layer were described by Martini forcefield,⁶³ which used four to one mapping, where four heavy atoms were grouped into one bead. In our simulation, to represent water contact angle (i.e., 110 °) on fully FOTS coated surface,⁶⁴ a new forcefield type for fluorinated carbon atoms was added by modifying forcefield from Mannelli et al.'s work.⁶⁵ Bond and angle potentials for FOTS molecule on SiO₂ surface were parameterized by comparing bond and angle probability distribution of all-atom, which used COMPASS forcefield,⁶⁶ and coarse-grained models. It is notable that FOTS attached to SiO₂ surface in a monodentate form was used in our simulation.

NVT simulation was performed for 60 ~ 155 ns with 20 fs timestep, and last 5 ns was analyzed for contact angle measurements. Temperature was controlled by Berendsen thermostat at 298 K. LAMMPS was used for simulations of contact angle measurement,⁶⁷ Forcite module in Material Studio was used for fitting the bonding potential of FOTS molecule.⁶⁸

To measure the contact angle of water droplet, density between liquid and vapor interface was divided by following equation

$$\rho(z) = \frac{1}{2}(\rho^l + \rho^v) - \frac{1}{2}(\rho^l - \rho^v) \tanh\left(\frac{2(z - z_e)}{d}\right) \quad (2.6)$$

where, $\rho(z)$ is the density profile across the interface; ρ^l and ρ^v are bulk liquid density and bulk vapor density; z_e , z , and d are the height of the equimolar dividing surface, the distance above the solid surface, and the thickness of interface, respectively. After liquid-vapor interface was fitted, we used circular fit equation for measurement of contact angle.

Figure 2.11 represents the cosine of the contact angles using CGMD simulation and interaction energy, E_{int} , versus pattern diameter/distance between patterns, D/L , at $D = 2$ nm which corresponds to $D = 80$ μm in the experimental systems. The simulation results show good agreement with the Cassie equation, which is same with the experimental results (Figure 2.2), except for $D/L = 0.5$. When D/L is 0.5, the experimental result agrees with the Cassie equation, but the simulation result disagrees with the Cassie equation and the experimental result. The reason for this is that in the simulation, the deposited FOTS is calculated to have full coverage, which results in a contact angle of 110 degrees, while the experiment cannot have full FOTS coverage, which results in a contact angle of 100 degrees. When the spacing is large, the coverage of FOTS does not have a considerable effect on the contact angle, but when spacings decrease, the FOTS-water interaction energy increases, which has a significant effect on the contact angle. Therefore, due to this coverage effect, it is assumed that the simulation values differ from the experimental values when D/L increases.

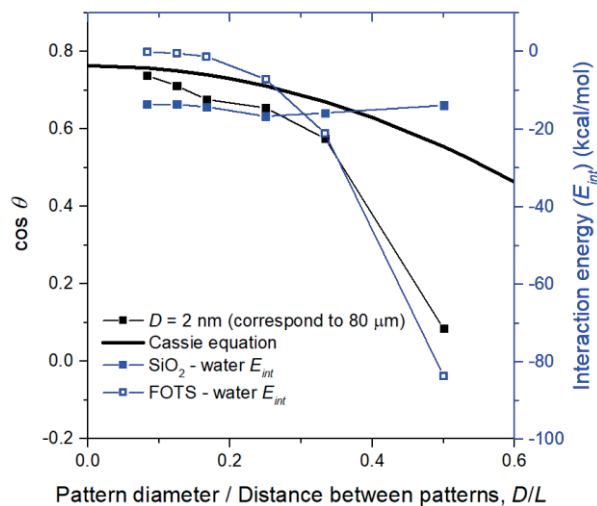


Figure 2.11. Cosine of the contact angles using CGMD simulation (represented by black) and interaction energy, E_{int} (represented by blue) versus pattern diameter/distance between patterns, D/L at $D = 2$ nm. Dashed curve corresponds to the Cassie equation. This simulation result is obtained in collaboration with professor Kwak's group.

Figure 2.12 shows water droplets deposited at different positions on a simulated surface with $D/L = 0.5$ for $D = 16.2$ nm, which corresponds to 640 μm in the experimental system. Like the experiment, the water droplet shape largely deviates from a circular shape, and Figure 2.12e shows a droplet shape that is similar with the experimental result (Figure 2.7i). Additionally, the contact angles of the

simulation are similar with the experimental result ($52.0 \pm 2.3^\circ$).

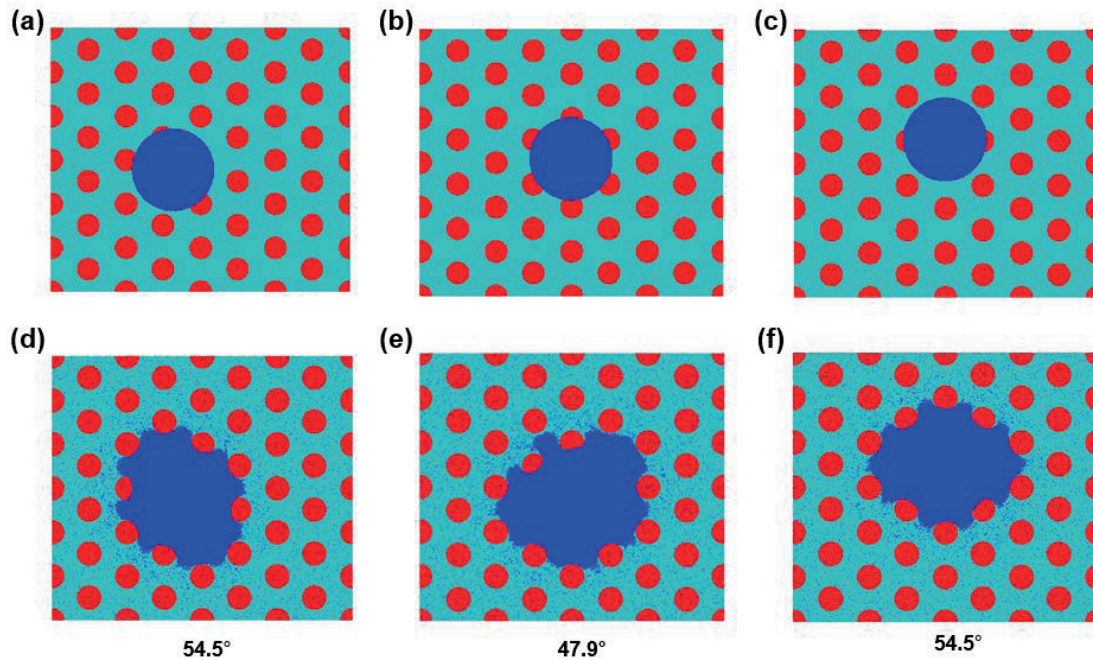


Figure 2.12. Water droplet morphology according to differing droplet positions. Initial model systems with D/L of 0.5 for $D = 16.2$ nm (which corresponds to $640 \mu\text{m}$ in the experimental system) depending on the initial position of the water droplets (a-c) and the water droplets after 100 ns (d-f). The final equilibrium contact angles are shown below. This simulation result is obtained in collaboration with professor Kwak's group.

Chapter 3. Robust superhydrophobic surfaces via Concave pillar

Robust superhydrophobic surfaces

Hydrophobic surfaces provide the water repellency property which allows water to be easily expelled, and this property is used in a vast amount of applications including self-cleaning,¹ anti-icing,⁸ anti-biofouling,³ anticorrosion,⁶⁹⁻⁷⁰ etc. This unique property is inspired by the lotus leaf,⁷¹ and this leaf provides low hysteresis and has inspired many artificial surfaces. This property is achieved by a layer of air under the liquid, and this state is referred to as the Cassie-Baxter state.³⁰ However, due to external pressure, vibration, droplet impact, and droplet evaporation, air layers can disappear or easily dissolve into water,⁷²⁻⁷⁴ so liquids penetrate into the pores and fully fill them. This state is referred to as the Wenzel state, where there no air layer under the liquid, and this surface has high hysteresis, so water is pinned on the surface.

In many applications, a sticky surface where the water is pinned on the solid surface and has limited mobility, is not desirable, so it is crucial to stabilize the air layer under the liquid. Also, there have been several structures developed to stabilize the air layer under the droplet, including doubly re-entrant pillars inspired by the skin of a springtail,⁷⁵⁻⁷⁷ doubly re-entrant inspired cavities,⁷⁸ a salvinia structure which has a hydrophilic tip on a hydrophobic pillar,⁷⁹⁻⁸⁰ etc. However, it is difficult to maintain the Cassie-Baxter state without fluorocarbon coating in pillars, and hard to fabricate the cavities structure. Hence, I found the pulvilli of the leaf beetle which have a concave-like structure and mimicked this structure. Herein, I developed a method to fabricate concave pillar structures and study the characteristics of these structures. The bioinspired concave pillar structures not only help to develop robust and stable superhydrophobic surfaces but also advance the understanding behind the Cassie Baxter to Wenzel transition phenomena.

Pulvilli of leaf beetle

Lepidoptera species have a well-developed palmula at the end of their tarsus for locomotion. Furthermore, Lepidoptera, Tettigonidae, and Coccinellidae families have a special organ called pulvilli that is located near the palmula which secretes an adhesive Bingham fluid. This organ has a unique microstructure that helps with their locomotion and helps to exclude contaminants. Lepidoptera species have evolved so their setae not only enhance their locomotion ability by expanding the interfacial surface of setae but also eliminate contaminants which can interrupt their efficient moving.

In particular, the setae that grow up on the pulvilli have concave-like structures (Figure 3.2 a-c). This microstructure contributes to the locomotion of the leaf beetle and has a self-cleaning function to remove contaminants that may interfere with movement.⁸¹ This unique and well-developed concave structure can help a biomimetic surface obtain the self-cleaning ability.

Concave pillar

In this work, we present a method to fabricate robust hydrophobic surfaces possessing a concave on the top of pillars by using lithographic and etching techniques (Figure 3.2). This success is attributed to wet etching using a potassium hydroxide (KOH) and isopropyl alcohol (IPA) solution, and then a nitric acid (HNO_3) and hydrogen fluoride (HF) solution,⁸² as well as Cr sputtering for the mask. A hexagonal array silicon dioxide mask is prepared by photolithography and dielectric ICP, and it is etched in using a KOH and IPA solution. KOH is used as the anisotropic etchant of silicon, where the (111) plane of silicon is etched more slowly than other planes, so silicon is etched in an inverted pyramid shape (Figure 3.1a). KOH can etch the photoresist, so silicon dioxide is used as a mask for KOH etching. When IPA is added to KOH etchant, the etch rate is decreased and concaves with a rounder surface and shallow bottoms can be obtained. Next, the isotropic etching process using a HNO_3 and HF solution makes the concaves round. After the KOH etching process, Cr is deposited on the surface, and then silicon dioxide is etched in buffered oxide etcher (BOE). Since the photoresist is peeled off in the BOE, Cr is used as a mask in the Bosch process. In the lift-off process, generally evaporation is used,⁸³ but in this work, sputtering is used for a high step coverage to cover the concave under the silicon dioxide. Finally, the sample is etched in the deep Si etcher and Cr is etched in the Cr etchant.

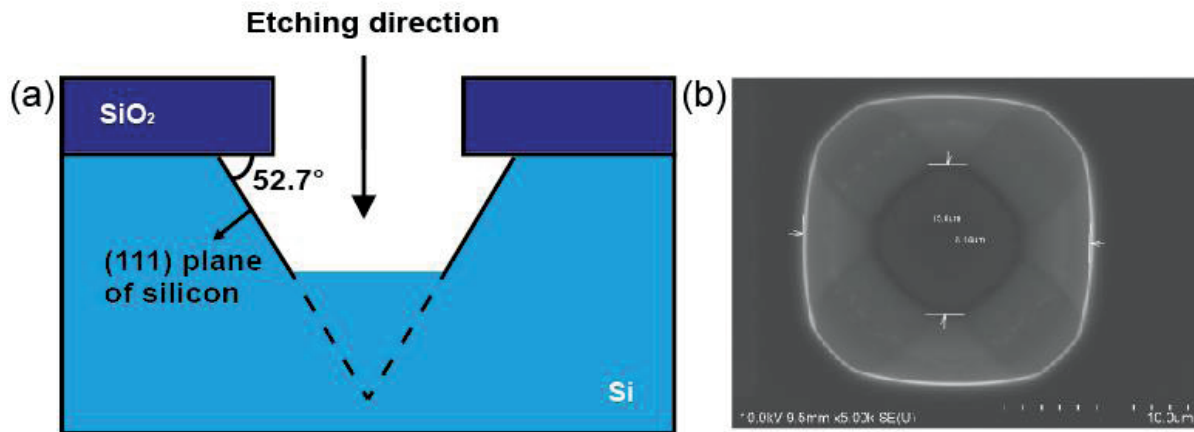


Figure 3.1. (a) Schematic of potassium hydroxide (KOH) etching. KOH etches the silicon but the (111) plane is etched at a slower rate. (b) FE-SEM image of a concave after KOH and isopropyl alcohol (IPA) solution etching followed by nitric acid (HNO₃) and hydrogen fluoride (HF) solution etching. The scale bar is 10 μm.

3.1 Experimental

Preparation of concave pillar. Figure 3.2d represents a schematic of the preparation of a concave pillar. A 4-inch silicon wafer (P-type, 100) was thermally oxidized to a thickness of 1.69 μm in the furnace (KHD-306, KSM). Afterwards, the wafer was immersed in a 3:1 sulfuric acid and 30% hydrogen peroxide solution for 30 min at 80 °C. Following this, it was rinsed using deionized (DI) water and dried using nitrogen gun. Photoresist (DPR-i1549) was spin coated on the silicon dioxide, and then the photoresist was baked, exposed to ultraviolet (UV) light (MA/BA6-8, Suss Microtec), and developed (AZ 300 MIF Developer). A dielectric ICP etcher (FABstar, TTL) etched silicon dioxide which was used as a mask for silicon etching. Silicon was etched using potassium hydroxide (KOH) and isopropyl alcohol (IPA) under four conditions.

- (i) 5M KOH + IPA (80:20 by volume ratio) at 70°C for 10 min
- (ii) 5M KOH + IPA (80:20 by volume ratio) at 70°C for 15 min
- (iii) 5M KOH + IPA (85:15 by volume ratio) at 70°C for 10 min
- (iv) 5M KOH + IPA (90:10 by volume ratio) at 70°C for 10 min

Wet etched silicon was rinsed using DI water and dried using a nitrogen gun, and then immersed in the 5:1 by volume ratio of pure nitric acid (HNO₃) to 40wt% hydrogen fluoride (HF) for 3 min to make the concave an inverted truncated sphere shape and rinsed using DI water and dried using a nitrogen gun.⁸²

Cr was deposited on the etched samples to a thickness of 4000 Å by using a DC sputter (SRN-120, SORONA). The lift-off process is conducted by an e-beam evaporator,⁸⁴ but in this experiment, the sputter was used to cover the silicon under the silicon dioxide due to difference in kinetic energy. Cr was used as a mask for silicon etching. Silicon dioxide was etched in buffered oxide etcher (BOE) solution for 10 min, and then silicon was etched by using a deep Si etcher (Tegal 200, Tegal France). The condition of the deep Si etcher is presented in Table 3.1. After Cr was etched in chromium etchant (Sigma Aldrich), FOTS was coated in the SAM coater (AVC – 150, SORONA).

Preparation of normal pillar. Photoresist (AZ nLOF2035) was spin coated on the silicon wafer. Following this, the photoresist was baked, exposed to ultraviolet (UV) light, and developed. Silicon was etched by using a deep Si etcher (Tegal 200, Tegal France). The normal pillar was also etched under the same conditions as the concave pillar in the deep Si etcher. Next, the wafer was immersed in the 3:1 of sulfuric acid and 30% hydrogen peroxide solution for 5 min at 80 °C, and then it was rinsed with DI water and dried using a nitrogen gun, and FOTS was coated in the SAM coater.

Table 3.1. Etching parameters of the Deep Si etcher.

	First cycle	Second cycle	Third cycle
Power (W)	3000	3000	3000
SF ₆ (sccm)	0	0	300
C ₄ F ₈ (sccm)	150	0	0
O ₂ (sccm)	0	80	0
Cycle time (second)	1	0.5	3
Total time (minute)	4 - 6		

Contact angle measurement. Before FOTS coating, water contact angles the concave pillars were measured by using a goniometer (DSA100-S, KRUSS) in at least five different positions on each sample for statistical analysis. DI water droplets with a volume of 6 μL hanging from the syringe were gently deposited on the samples. Contact angles were measured parallel to the rows because contact angles differ according to the viewing angle.⁵⁸

Field Emission Scanning Electron Microscope (FE-SEM). The shape of concave pillars and normal pillars, as well as the depth of a concave and the height of pillars were observed by using a FE-SEM (Hitachi S-4800, Hitachi).

Air injection test. DI water was poured into the beaker and samples were immersed in water. In the Cassie-Baxter state, the trapped air reflects light, so samples were observed to be a bright silver color. Then, air is repeatedly injected on the surface of samples. In the Wenzel state, there is no trapped air, so samples were observed to be dark.⁸⁰

Cassie-Baxter to Wenzel Transition rate measurement. Optical microscopy (Edmund Optics) was used to observe the transition from the Cassie-Baxter state to the Wenzel state. DI water is poured into glass chamber (coated by FOTS), and then samples were put into the glass chamber gently. Next, this glass chamber was placed under the microscope. It took 10 seconds to rearrange the sample and focus the sample after samples were immersed in water. For the first 10 minutes, images were taken at 1 frame per second, and then at 1 frame per 5 minutes. The Cassie-Baxter to Wenzel transition is recorded for 24 hours. Each image is analyzed using Image J. When the sample is in the Cassie-Baxter state, it is seen as bright, but when the sample is in Wenzel state, it is seen as dark. The edge of the sample and the generated air bubbles were excluded from the analysis. To avoid the influence of temperature, this experiment was conducted in a room where temperature and humidity were maintained.

Dissolved air concentration control. 0% aerated water was prepared using a glass vial and Teflon tape. DI water was poured into the glass vial, and then Teflon tape and a magnetic bar were put into the glass vial. The glass vial was placed on a stirring plate while a vacuum was applied for 2 hours inside the vial. Aerated water was prepared using argon gas. The DI water in the glass vial was in contact with argon gas for 2 hours.

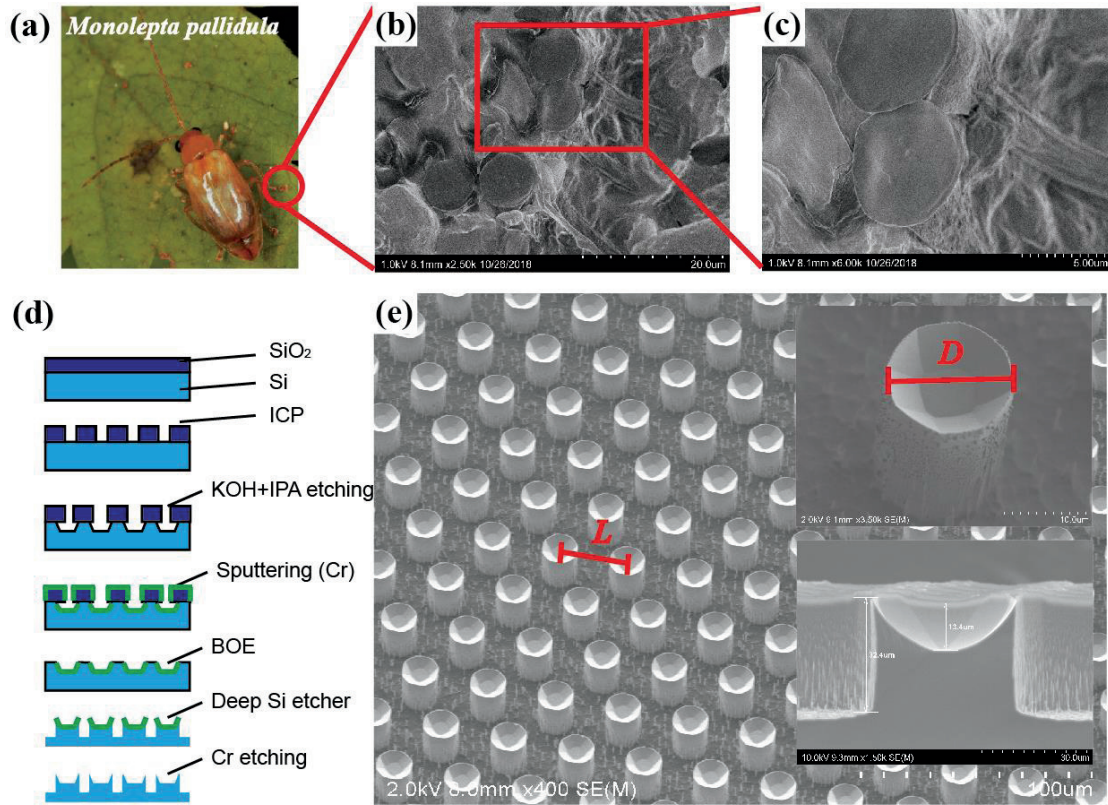


Figure 3.2. (a-c) Photograph of a leaf beetle insect, and field emission scanning electron microscope (FE-SEM) image of a pulvilli of the leaf beetle with a concave structure. Scale bars are 20 μm and 10 μm , respectively. (d) Schematic of the preparation of a concave pillar. (e) FE-SEM image of the concave pillar. The insets are a magnification of the concave pillar and a cross section of the concave pillar. Scale bars are 100 μm for the image, and 10 μm and 30 μm in the insets, respectively.

3.2 Results and Discussion

Figure 3.2e shows an FE-SEM image of a fabricated concave pillar using anisotropic etching and the Bosch process. Anisotropic etching of the silicon was conducted under four conditions. FE-SEM is used to identify the concave shape according to the anisotropic etching condition. Figure 3.3 and Table 3.2 show the depths (T) and diameters of the concave pillars (D), respectively. The FE-SEM images show similar depths of 15.1, 13.4, 13.9, 14.3 μm when the samples are anisotropically etched with IPA 10%, 15%, and 20% for 10 minutes and 20% for 15 minutes, respectively. Moreover, table 3.2 shows that the etching conditions have no significant effect on the diameter. The small differences in diameter occur as a result of deposition varying depending on position during sputtering because the sputter guns are tilted, or due to random error that occurs when the sample is stirred while immersed in the HNO_3 and HF solution. Therefore, the etching conditions have little influence on the diameter and depth of the concaves. However, to better understand the effects of etchant concentration and etching time on a concave pillar, samples need to be prepared while varying the IPA amount and etching time. Additionally, the angles and other shape properties of the concave will need to be further analyzed.

Table 3.2. Diameters of the concave pillars.

Mask size		Anisotropic etching with IPA 10% by volume ratio	Anisotropic etching with IPA 15% by volume ratio	Anisotropic etching with IPA 20% by volume ratio	Anisotropic etching with IPA 20% by volume ratio, 15 min
D (μm)	L (μm)	D (μm)	D (μm)	D (μm)	D (μm)
10	30	24	23.9	19.6	22.9
10	40	26	26.3	20.3	26.5
10	80	32.4	28.9	26.7	29.9
10	120	30.2	30.6	26.9	30.3
20	40	33.8	33.3	29	31
20	60	38.8	35.9	32.2	34.2
20	80	39	38	43.3	37.2
20	120	43.2	42.3	38	43.7
20	160	44.7	42.1	37.5	45.1
20	240	45.1	43	38.3	45.2

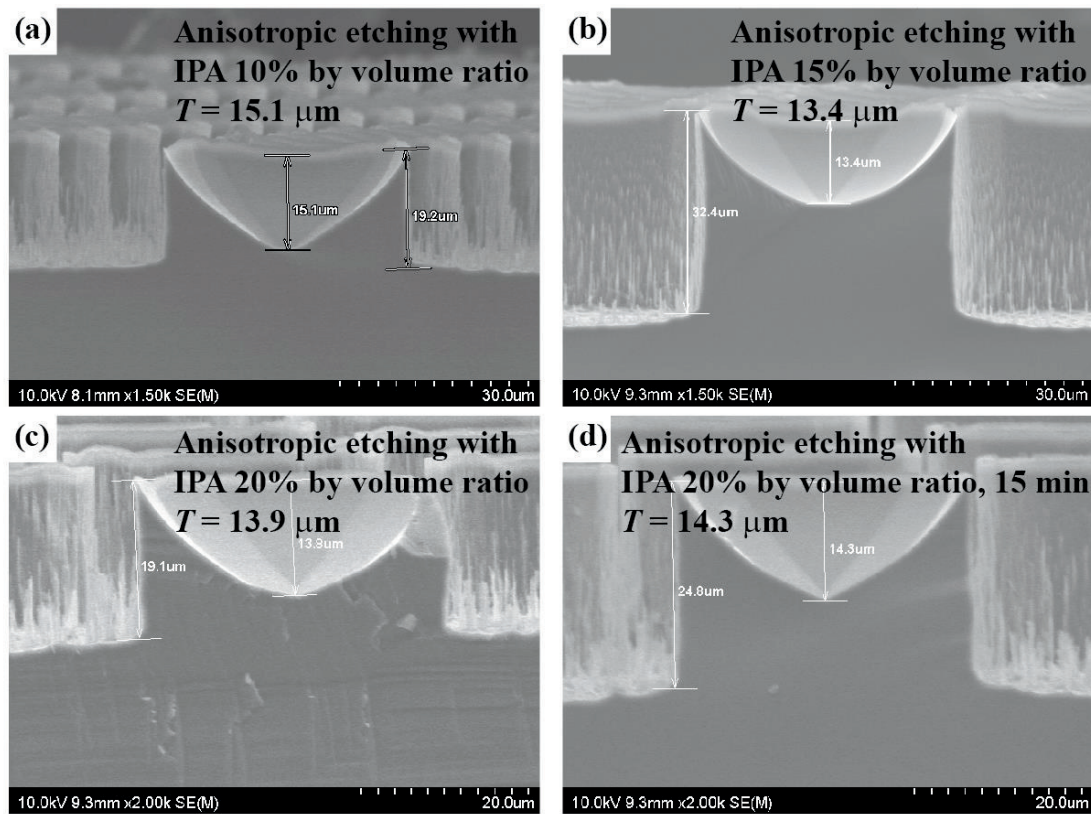

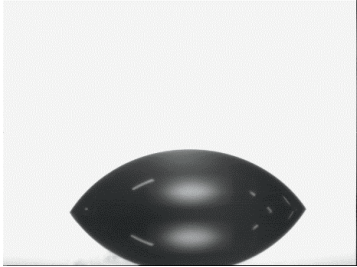

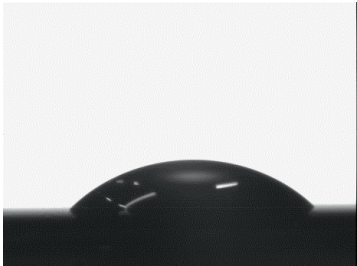


Figure 3.3. FE-SEM images of concave pillar according to the etching conditions. The concave pillar etched with IPA 10% (a), 15% (b) and 20% for 10 minutes (c) and 20% for 15 minutes (d), respectively.

To compare the properties of the normal pillar and the concave pillar, the water contact angles were measured before FOTS coating (Figure 3.4). Due to the differences in the processing of normal pillars and concave pillars, the intrinsic contact angle needs to be measured first, so flat silicon wafers were immersed in piranha solution (used to remove the photoresist from normal pillars) and Cr etchant (used to etch Cr from concave pillars). The surface chemistry is thought to be similar because both the piranha solution and the Cr etchant oxidize the silicon surface and form a thin layer of silicon dioxide. The intrinsic contact angles of the silicon wafers 2 days after the immersion process in piranha solution and Cr etchant are $63.3 \pm 2.6^\circ$ (in the case of normal pillar) and $46.9 \pm 0.4^\circ$ (in the case of concave pillar). These values are used to obtain the Cassie-Baxter and Wenzel angles. Theoretical values of the concave pillar are obtained with the assumption that it is a normal pillar, so the actual values of the Cassie-Baxter equation and Wenzel equation are smaller than the graph (represented by the blue solid and dashed curves, respectively) due to the concave area.

Table 3.3. Intrinsic contact angles.

	After the process	2 days after the process
Si after immersion in the piranha solution (normal pillar)	 $10.0 \pm 3.3^\circ$	 $63.3 \pm 2.6^\circ$
Si after immersion in the Cr etchant (concave pillar)	 $<5^\circ$	 $46.9 \pm 0.4^\circ$

When measuring the contact angles of pillars, most concave pillars maintain the Cassie-Baxter state, while many normal pillars with low D/L partially transitioned to the Wenzel state. Another point is that at high D/L , the experimental contact angles are higher than the theoretical Cassie-Baxter angles for the concave pillars. This is because previous processing steps can also affect the surface chemistry and increase the intrinsic contact angle. Especially contact angles of concave pillars are higher than the Cassie-Baxter equation when intrinsic contact angle is 110° . It seems that the inside of the concave might not fully wet, so it requires additional experiments to observe the meniscus of the water droplet on the concave by using the confocal microscopy. The confocal microscopy lens will be immersed in a water droplet mixed with a fluorescent material and observe the meniscus of the water droplet on the concave.

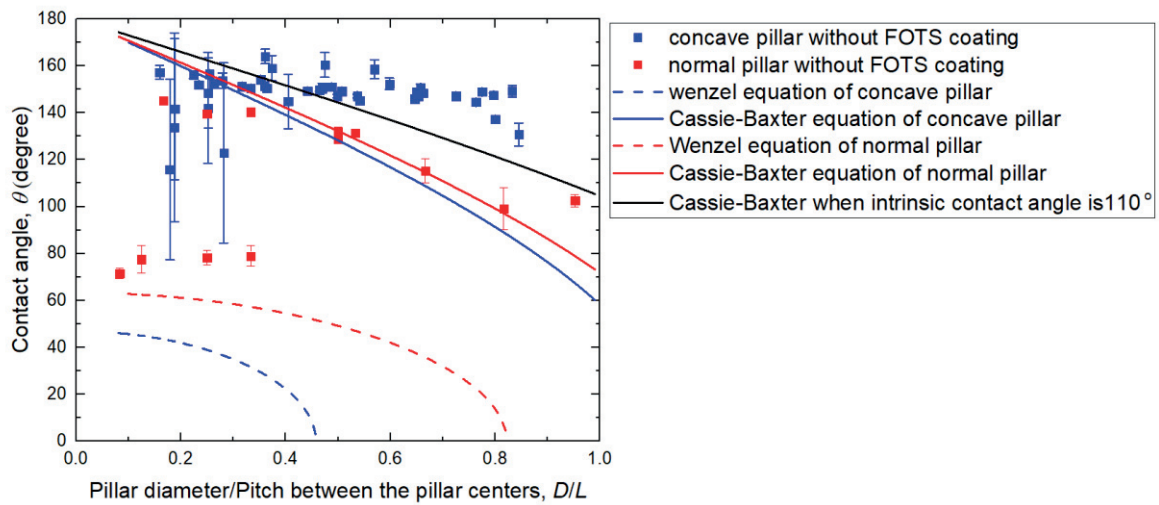


Figure 3.4. Measured contact angles versus pattern diameter/pitch between pillar centers, D/L , of the normal pillar (represented by red color) and the concave pillar (represented by blue color). Each point is the averaged value of at least five different positions and the error bars indicate the standard deviation. Red, blue, and black solid curves correspond to the Cassie-Baxter equation of normal pillar, concave pillar and when the intrinsic contact angle is 110° , respectively. Red and blue dashed curves correspond to the Wenzel equation of the normal pillar and concave pillar, respectively.

The contact angle results show that the concave pillar has a higher contact angle and better maintains the Cassie-Baxter state, so to better understand the underwater wettability, FOTS coated normal pillar and concave pillar samples were immersed in water. Figure 3.5 shows that when both samples are first immersed in water, they maintain the Cassie-Baxter state, shown by a bright silver color. While immersed in water, the normal pillar shows a transition to the Wenzel state after a few air injections, while the concave pillar maintains the Cassie-Baxter state even with multiple air injections. Therefore, even with fluctuation, the concave pillar better retains air compared to the normal pillar.

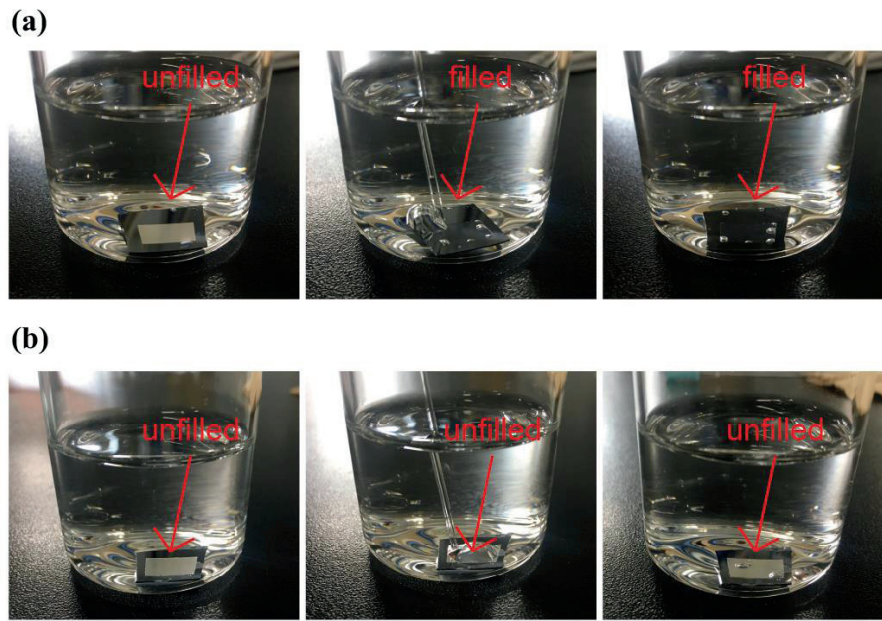


Figure 3.5. Underwater air injection test for the normal pillar (a), the concave pillar (b). The Cassie-Baxter state is maintained for the concave pillar during the air injection.

To investigate the transition rate for normal pillars and concave pillars immersed in water according to the aeration, samples immersed in water were observed through OM in a room with controlled temperature and humidity. During the observation, the edges of the sample, any air bubbles that formed on the surface, and the area where the transition occurred immediately due to defects were not considered for the analysis of the transition area. The concave pillar used in this experiment was etched in IPA 15 % by volume ratio, and the height of the pillars are 23.7 and 32.4 μm for the normal pillar and the concave pillar, respectively. The diameters of the pillars are 40 and 38 μm for the normal pillar and the concave pillar, respectively, and the pitch between the pillar centers for both samples is 80 μm (Figure 3.6). Since the edges of both pillars are completely covered, air is unable to pass through from the side (Figure 3.7). However, there are few applications where the edges are covered, so one of the sides was cut to allow air to pass through for both pillars (Figure 3.8b).

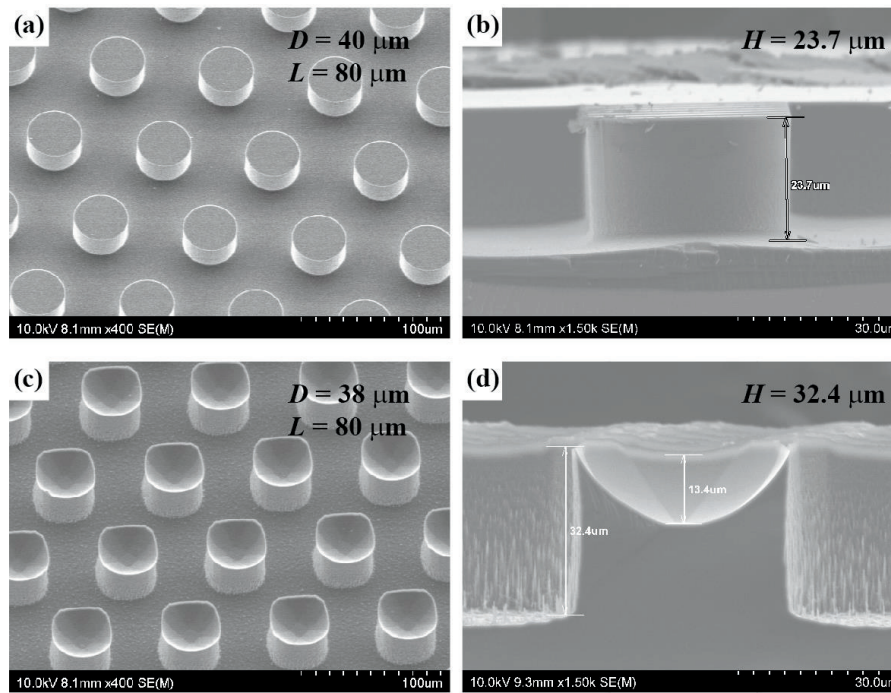


Figure 3.6. FE-SEM images of the normal pillar (a, b) and the concave pillar (c, d) used in Cassie-Baxter to Wenzel transition rate experiment.

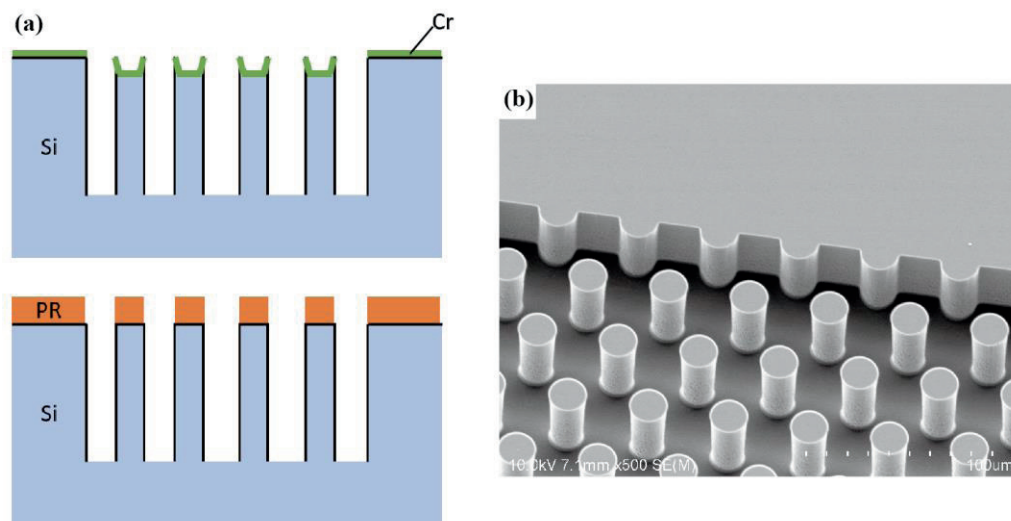


Figure 3.7. (a) Schematic of the concave pillar and normal pillar with covered edges. (b) FE-SEM image of the normal pillar edge.

Figure 3.8 shows the transition fraction versus time graph for the normal pillar and the concave pillar, and the images show the samples immersed in water with various aeration levels every 6 hours. Without the FOTS coating, the normal pillar has a contact angle of $131.8 \pm 1.9^\circ$, and the concave pillar has a contact angle of $160.4 \pm 5.3^\circ$. In the case of the normal pillar, as soon as it is immersed in 100% aerated water, it enters the Wenzel state, but the concave pillar only transitions 9.8% to the Wenzel state after 24 hours.

With the FOTS coating, the normal pillar immersed in 100% aerated water transitions 65.7% after 24 hours, and in 0% aerated water, it transitions 84.4% after 24 hours. In contrast, the concave pillar only transitions to the Wenzel state in the edges of the sample, which are excluded in the analysis, so the concave pillar immersed in both aerated and 0% aerated water maintains the Cassie-Baxter state for 24 hours. It seems that in the case of the concave pillar, water fill the concave instead of the gaps between pillars, so the concave pillar maintains the Cassie-Baxter state. However, more analysis is required to make sure of the air retention mechanism of concave pillars by using confocal microscopy and to immerse the concave pillar in the 0% aerated water for more than 24 hours to observe the stability of the air layer.

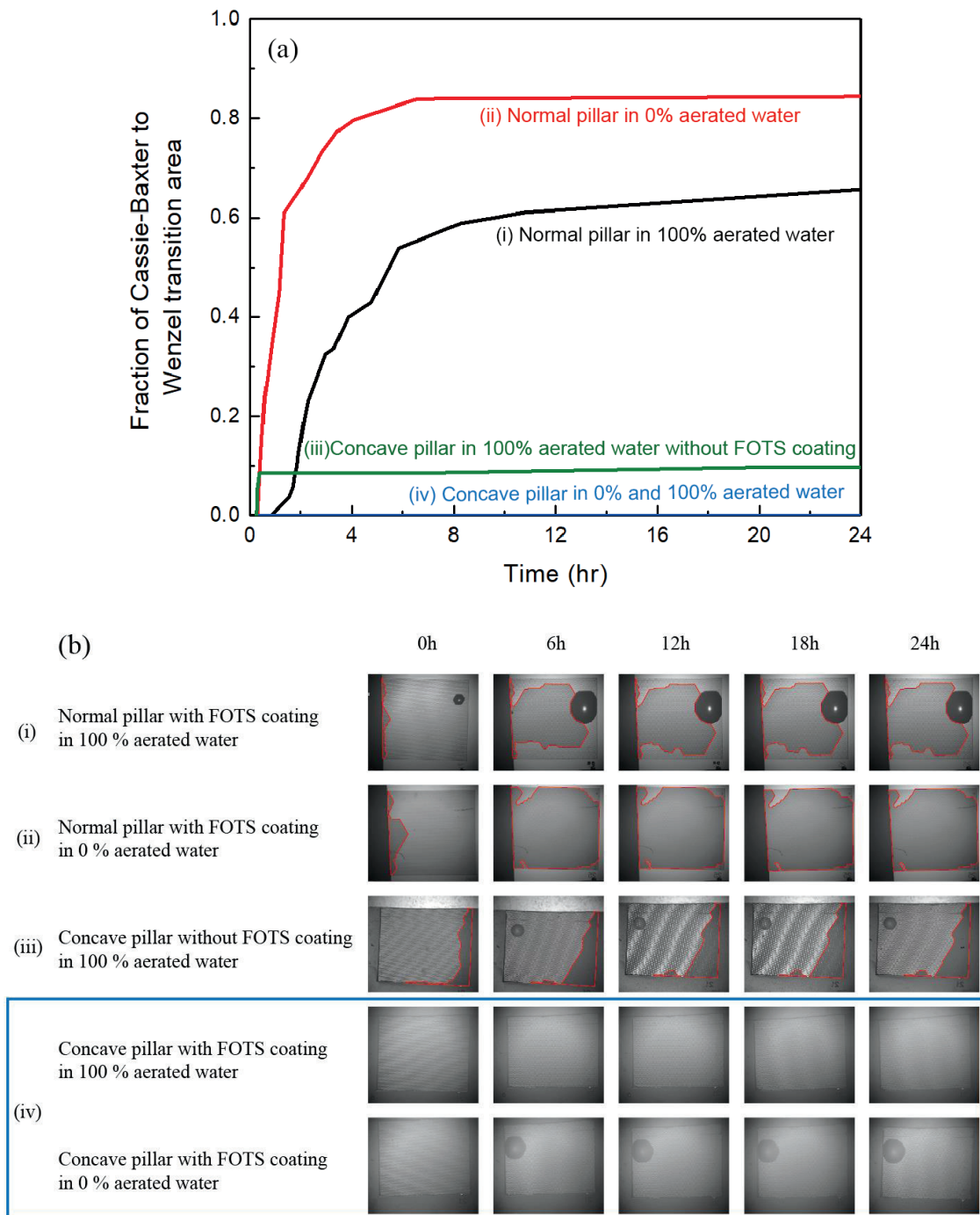


Figure 3.8. Cassie-Baxter to Wenzel transition rate of normal pillars and concave pillars. (a) Plot of fraction of Cassie-Baxter to Wenzel transition area versus time. (b) OM images of normal pillars and concave pillars immersed in water during the Cassie-Baxter to Wenzel transition rate experiment.

3.3 Conclusion

In Chapter 3 fabrication method for robust hydrophobic surfaces possessing a concave on the top of pillars inspired by the structure of leaf beetle pulvilli is presented and the characteristics are analyzed. Concaves have similar depths, and there is no tendency in diameter, so the etching conditions have no significant effect on the shape of the concave. When measuring the contact angles of pillars, most concave pillars maintain the Cassie-Baxter state, while many normal pillars with low D/L partially transitioned to the Wenzel state. Moreover, at high D/L , the inside of the concave might not fully wet, so it appears to have higher contact angles than the theoretical values when intrinsic contact angle is 110° . Furthermore, with fluctuation, the concave pillar better retains air compared to the normal pillar, and the concave pillar with FOTS coating maintains the Cassie-Baxter state for 24 hours in the water regardless of aeration.

The bioinspired concave pillar structures not only help to develop robust and stable superhydrophobic surfaces but also advance the understanding of the Cassie Baxter to Wenzel transition phenomena. However, a stability test is needed that is longer than 24 hours and more analysis to observe the meniscus of the water droplet on the concave by using the confocal microscopy is required to understand the air retention mechanism of concave pillars.

Chapter 4. Summary

In this work, wetting phenomena is studied historically, fundamentally, and from an application perspective. Since studies on wetting phenomena began in the 18th century, many developments have been made in various applications, measurement methods for wettability, equations predicting contact angles, and contact angle hysteresis.

Based on the studies on historical wetting phenomena, we investigated the fundamentals of smooth, flat, and chemically heterogeneous surfaces to revisit the Cassie equation. When water droplets with volumes of 6 μL are deposited on heterogeneous surfaces having diameters of 640 μm , the measured contact angles largely deviate from the Cassie equation, and the droplet shape deviates from a circular shape. Moreover, when water droplets with volumes of 6 μL are deposited on the heterogeneous surfaces having a diameter of 80 μm , the water droplets have a hexagonal shape.

With this fundamental knowledge, robust hydrophobic surfaces possessing a concave on the top of pillars inspired by the structure of leaf beetle pulvilli are investigated for application purposes. The concave pillar can be fabricated using photolithography, anisotropic etching of silicon, and using a Cr mask for deep Si etching. Concave pillar structures have excellent superhydrophobicity and stability in the Cassie-Baxter state compared to normal pillar structures.

This work provides a better understanding of the fundamental wetting phenomena of liquids and of the criteria of the Cassie equation. In addition, the bio-inspired concave pillar structures not only help to develop stable superhydrophobic surfaces but also to advance the understanding of the Cassie Baxter to Wenzel transition phenomena. However, contact angles will need to be compared with the modified Cassie equation which includes line fractions. Furthermore, a stability test longer than 24 hours and an experiment to observe the meniscus of the water droplet by using confocal microscopy are needed.

Chapter 5. Reference

1. Blossey, R., Self-cleaning surfaces — virtual realities. *Nature Materials* **2003**, 2 (5), 301-306.
2. Choi, W.; Tuteja, A.; Chhatre, S.; Mabry, J. M.; Cohen, R. E.; McKinley, G. H., Fabrics with Tunable Oleophobicity. *Advanced Materials* **2009**, 21 (21), 2190-2195.
3. Leslie, D. C.; Waterhouse, A.; Berthet, J. B.; Valentin, T. M.; Watters, A. L.; Jain, A.; Kim, P.; Hatton, B. D.; Nedder, A.; Donovan, K.; Super, E. H.; Howell, C.; Johnson, C. P.; Vu, T. L.; Bolgen, D. E.; Rifai, S.; Hansen, A. R.; Aizenberg, M.; Super, M.; Aizenberg, J.; Ingber, D. E., A bioinspired omniphobic surface coating on medical devices prevents thrombosis and biofouling. *Nat Biotech* **2014**, 32 (11), 1134-1140.
4. Nakashima, Y.; Nakanishi, Y.; Yasuda, T., Automatic droplet transportation on a plastic microfluidic device having wettability gradient surface. *Rev Sci Instrum* **2015**, 86 (1), 015001.
5. Zheng, Y.; Cheng, J.; Zhou, C.; Xing, H.; Wen, X.; Pi, P.; Xu, S., Droplet Motion on a Shape Gradient Surface. *Langmuir* **2017**, 33 (17), 4172-4177.
6. Matsubayashi, T.; Tenjimbayashi, M.; Komine, M.; Manabe, K.; Shiratori, S., Bioinspired Hydrogel-Coated Mesh with Superhydrophilicity and Underwater Superoleophobicity for Efficient and Ultrafast Oil/Water Separation in Harsh Environments. *Industrial & Engineering Chemistry Research* **2017**, 56 (24), 7080-7085.
7. Sawane, Y. B.; Ogale, S. B.; Banpurkar, A. G., Low Voltage Electrowetting on Ferroelectric PVDF-HFP Insulator with Highly Tunable Contact Angle Range. *ACS Appl Mater Interfaces* **2016**, 8 (36), 24049-56.
8. Golovin, K.; Kobaku, S. P. R.; Lee, D. H.; DiLoreto, E. T.; Mabry, J. M.; Tuteja, A., Designing durable icephobic surfaces. *Science Advances* **2016**, 2 (3), e1501496.
9. Xu, W.; Lu, Z.; Wan, P.; Kuang, Y.; Sun, X., High-Performance Water Electrolysis System with Double Nanostructured Superaerophobic Electrodes. *Small* **2016**, 12 (18), 2492-2498.
10. He, J.; Hu, B.; Zhao, Y., Superaerophobic Electrode with Metal@Metal-Oxide Powder Catalyst for Oxygen Evolution Reaction. *Advanced Functional Materials* **2016**, 26 (33), 5998-6004.
11. de Laplace P.S., *Mecanique Celeste*, Suppl. au Xieme Livre, L'ouvier, Paris **1805**.
12. Poisson S.D., *Nouvelle Theorie de L'action Capillaire*, Paris **1831**.
13. Young, T., An Essay on the Cohesion of Fluids. *Philosophical Transactions of the Royal Society of London* **1805**, 95 (0), 65-87.
14. *The Collected Works of J. Williard Gibbs*, Yale University press, London 1957.
15. Wiese, H., A. W. Adamson: "Physical Chemistry of Surfaces", 5. Auflage, John Wiley & Sons Inc., New York, Chichester, Brisbane, Toronto, Singapore 1990. 777 Seiten, Preis: £ 47.50. *Berichte der*

Bunsengesellschaft für physikalische Chemie **1991**, 95 (6), 758-758.

16. Drelich, J., Static contact angles for liquids at heterogeneous rigid solid surfaces. *Polish Journal of Chemistry* **1997**, 71 (5), 525-549.

17. Blokhuis, E. M.; Shilkrot, Y.; Widom, B., Young's law with gravity. *Molecular Physics* **1995**, 86 (4), 891-899.

18. Jurin, J., II. An account of some experiments shown before the Royal Society; with an enquiry into the cause of the ascent and suspension of water in capillary tubes. *Philosophical Transactions* **1719**, 30 (355), 739-747.

19. Jurin, J., II. An account of some new experiments, relating to the action of glass tubes upon water and quicksilver. *Philosophical Transactions* **1719**, 30 (363), 1083-1096.

20. L.A. Wilhelmy, *Ann. Phys.* **1863**, 119, 117.

21. F. Bashforth, J.C. Adams, *An Attempt to Test the Theory of Capillary Action*, Cambridge, London, **1892**.

22. Blaisdell, B. E., The Physical Properties of Fluid Interfaces of Large Radius of Curvature. I. Integration of LaPlace's Equation for the Equilibrium Meridian of a Fluid Drop of Axial Symmetry in a Gravitational Field. Numerical Integration and Tables for Sessile Drops of Moderately Large Size. *Journal of Mathematics and Physics* **1940**, 19 (1-4), 186-216.

23. Fordham, S., On the calculation of surface tension from measurements of pendant drops. *Proceedings of the Royal Society of London. Series A. Mathematical and Physical Sciences* **1948**, 194 (1036), 1-16.

24. Rotenberg, Y.; Boruvka, L.; Neumann, A. W., Determination of surface tension and contact angle from the shapes of axisymmetric fluid interfaces. *Journal of Colloid and Interface Science* **1983**, 93 (1), 169-183.

25. Cheng, P.; Li, D.; Boruvka, L.; Rotenberg, Y.; Neumann, A. W., Automation of axisymmetric drop shape analysis for measurements of interfacial tensions and contact angles. *Colloids and Surfaces* **1990**, 43 (2), 151-167.

26. Río, O. I. d.; Neumann, A. W., Axisymmetric Drop Shape Analysis: Computational Methods for the Measurement of Interfacial Properties from the Shape and Dimensions of Pendant and Sessile Drops. *Journal of Colloid and Interface Science* **1997**, 196 (2), 136-147.

27. Yuan, Y.; Lee, T. R., Contact Angle and Wetting Properties. In *Surface Science Techniques*, Bracco, G.; Holst, B., Eds. Springer Berlin Heidelberg: Berlin, Heidelberg, 2013; pp 3-34.

28. Cassie, A. B. D., Contact angles. *Discussions of the Faraday Society* **1948**, 3.

29. Wenzel, R. N., RESISTANCE OF SOLID SURFACES TO WETTING BY WATER. *Industrial & Engineering Chemistry* **1936**, 28 (8), 988-994.

30. Cassie, A. B. D.; Baxter, S., Wettability of porous surfaces. *Transactions of the Faraday Society* **1944**, *40* (0), 546-551.
31. Drelich, J.; Miller, J. D., Modification of the Cassie equation. *Langmuir* **1993**, *9* (2), 619-621.
32. Israelachvili, J. N.; Gee, M. L., Contact angles on chemically heterogeneous surfaces. *Langmuir* **1989**, *5* (1), 288-289.
33. Hey, M. J.; Kingston, J. G., The apparent contact angle for a nearly spherical drop on a heterogeneous surface. *Chemical Physics Letters* **2007**, *447* (1-3), 44-48.
34. Larsen, S. T.; Taboryski, R., A Cassie-Like Law Using Triple Phase Boundary Line Fractions for Faceted Droplets on Chemically Heterogeneous Surfaces. *Langmuir* **2009**, *25* (3), 1282-1284.
35. Swain, P. S.; Lipowsky, R., Contact Angles on Heterogeneous Surfaces: A New Look at Cassie's and Wenzel's Laws. *Langmuir* **1998**, *14* (23), 6772-6780.
36. Xu, X.; Wang, X., The modified Cassie's equation and contact angle hysteresis. *Colloid and Polymer Science* **2012**, *291* (2), 299-306.
37. Iwamatsu, M., The validity of Cassie's law: a simple exercise using a simplified model. *J Colloid Interface Sci* **2006**, *294* (1), 176-81.
38. Suzuki, S.; Ueno, K., Apparent Contact Angle Calculated from a Water Repellent Model with Pinning Effect. *Langmuir* **2017**, *33* (1), 138-143.
39. Kang, H. C.; Jacobi, A. M., Equilibrium Contact Angles of Liquid Droplets on Ideal Rough Solids. *Langmuir* **2011**, *27* (24), 14910-14918.
40. Krumpfer, J. W.; McCarthy, T. J., Contact angle hysteresis: a different view and a trivial recipe for low hysteresis hydrophobic surfaces. *Faraday Discussions* **2010**, *146* (0), 103-111.
41. Gao, L.; McCarthy, T. J., Contact Angle Hysteresis Explained. *Langmuir* **2006**, *22* (14), 6234-6237.
42. Bliznyuk, O.; Vereshchagina, E.; Kooij, E. S.; Poelsema, B., Scaling of anisotropic droplet shapes on chemically stripe-patterned surfaces. *Phys Rev E Stat Nonlin Soft Matter Phys* **2009**, *79* (4 Pt 1), 041601.
43. Gao, L.; McCarthy, T. J., How Wenzel and Cassie were wrong. *Langmuir* **2007**, *23* (7), 3762-5.
44. Extrand, C. W., Contact Angles and Hysteresis on Surfaces with Chemically Heterogeneous Islands. *Langmuir* **2003**, *19* (9), 3793-3796.
45. Bormashenko, E., A variational approach to wetting of composite surfaces: is wetting of composite surfaces a one-dimensional or two-dimensional phenomenon? *Langmuir* **2009**, *25* (18), 10451-4.
46. Extrand, C. W.; Moon, S. I., Which controls wetting? Contact line versus interfacial area: simple experiments on capillary rise. *Langmuir* **2012**, *28* (44), 15629-33.
47. Cubaud, T.; Fermigier, M., Advancing contact lines on chemically patterned surfaces. *Journal of Colloid and Interface Science* **2004**, *269* (1), 171-177.

48. Li, R.; Shan, Y., Contact angle and local wetting at contact line. *Langmuir* **2012**, *28* (44), 15624-8.
49. Mierczynska, A.; Micheltore, A.; Tripathi, A.; Goreham, R. V.; Sedev, R.; Vasilev, K., pH-tunable gradients of wettability and surface potential. *Soft Matter* **2012**, *8* (32), 8399-8404.
50. Varagnolo, S.; Ferraro, D.; Fantinel, P.; Pierno, M.; Mistura, G.; Amati, G.; Biferale, L.; Sbragaglia, M., Stick-Slip Sliding of Water Drops on Chemically Heterogeneous Surfaces. *Physical Review Letters* **2013**, *111* (6), 066101.
51. Wang, J.; Bratko, D.; Luzar, A., Probing surface tension additivity on chemically heterogeneous surfaces by a molecular approach. *Proceedings of the National Academy of Sciences* **2011**, *108* (16), 6374-6379.
52. Brandon, S.; Haimovich, N.; Yeager, E.; Marmur, A., Partial wetting of chemically patterned surfaces: The effect of drop size. *Journal of Colloid and Interface Science* **2003**, *263* (1), 237-243.
53. Carmeliet, J.; Chen, L.; Kang, Q.; Derome, D., Beyond-Cassie Mode of Wetting and Local Contact Angles of Droplets on Checkboard-Patterned Surfaces. *Langmuir* **2017**, *33* (24), 6192-6200.
54. Zhang, K.; Chen, S.; Wang, Y., Ratio dependence of contact angle for droplet wetting on chemically heterogeneous substrates. *Colloids and Surfaces A: Physicochemical and Engineering Aspects* **2018**, *539*, 237-242.
55. Ruiz-Cabello, F. J.; Kusumaatmaja, H.; Rodriguez-Valverde, M. A.; Yeomans, J.; Cabrerizo-Vilchez, M. A., Modeling the corrugation of the three-phase contact line perpendicular to a chemically striped substrate. *Langmuir* **2009**, *25* (14), 8357-61.
56. Zhang, B.; Wang, J.; Liu, Z.; Zhang, X., Beyond Cassie equation: local structure of heterogeneous surfaces determines the contact angles of microdroplets. *Sci Rep* **2014**, *4*, 5822.
57. Woodward, J. T.; Gwin, H.; Schwartz, D. K., Contact Angles on Surfaces with Mesoscopic Chemical Heterogeneity. *Langmuir* **2000**, *16* (6), 2957-2961.
58. Kashaninejad, N.; Nguyen, N.-T.; Chan, W. K., The three-phase contact line shape and eccentricity effect of anisotropic wetting on hydrophobic surfaces. *Soft Matter* **2013**, *9* (2), 527-535.
59. Calvert, P., Inkjet Printing for Materials and Devices. *Chemistry of Materials* **2001**, *13* (10), 3299-3305.
60. Park, B. K.; Kim, D.; Jeong, S.; Moon, J.; Kim, J. S., Direct writing of copper conductive patterns by ink-jet printing. *Thin Solid Films* **2007**, *515* (19), 7706-7711.
61. Cubaud, T.; Fermigier, M., Faceted drops on heterogeneous surfaces. *Europhysics Letters* **2001**, *55* (2), 239-245.
62. Marmur, A.; Bittoun, E., When Wenzel and Cassie are right: reconciling local and global considerations. *Langmuir* **2009**, *25* (3), 1277-81.
53. Marrink, S. J.; Risselada, H. J.; Yefimov, S.; Tieleman, D. P.; de Vries, A. H., The MARTINI Force

Field: Coarse Grained Model for Biomolecular Simulations. *The Journal of Physical Chemistry B* **2007**, *111* (27), 7812-7824.

64. Ashurst, W. R.; Carraro, C.; Maboudian, R., Vapor phase anti-stiction coatings for MEMS. *IEEE Transactions on Device and Materials Reliability* **2003**, *3* (4), 173-178.

65. Mannelli, I.; Sagués, F.; Pruneri, V.; Reigada, R., Lipid Vesicle Interaction with Hydrophobic Surfaces: A Coarse-Grained Molecular Dynamics Study. *Langmuir* **2016**, *32* (48), 12632-12640.

66. Sun, H., COMPASS: An ab Initio Force-Field Optimized for Condensed-Phase Applications Overview with Details on Alkane and Benzene Compounds. *The Journal of Physical Chemistry B* **1998**, *102* (38), 7338-7364.

67. Plimpton, S., Fast Parallel Algorithms for Short-Range Molecular Dynamics. *Journal of Computational Physics* **1995**, *117* (1), 1-19.

68. Dassault Systèmes BIOVIA, Materials Studio 2018, San Diego: Dassault Systèmes, 2018.

69. Su, F.; Yao, K., Facile Fabrication of Superhydrophobic Surface with Excellent Mechanical Abrasion and Corrosion Resistance on Copper Substrate by a Novel Method. *ACS Applied Materials & Interfaces* **2014**, *6* (11), 8762-8770.

70. Zhao, K.; Liu, K. S.; Li, J. F.; Wang, W. H.; Jiang, L., Superamphiphobic CaLi-based bulk metallic glasses. *Scripta Materialia* **2009**, *60* (4), 225-227.

71. Barthlott, W.; Neinhuis, C., Purity of the sacred lotus, or escape from contamination in biological surfaces. *Planta* **1997**, *202* (1), 1-8.

72. Papadopoulos, P.; Mammen, L.; Deng, X.; Vollmer, D.; Butt, H.-J., How superhydrophobicity breaks down. *Proceedings of the National Academy of Sciences* **2013**, *110* (9), 3254-3258.

73. Whyman, G.; Bormashenko, E., How to Make the Cassie Wetting State Stable? *Langmuir* **2011**, *27* (13), 8171-8176.

74. Bobji, M. S.; Kumar, S. V.; Asthana, A.; Govardhan, R. N., Underwater Sustainability of the “Cassie” State of Wetting. *Langmuir* **2009**, *25* (20), 12120-12126.

75. Choi, J.; Jo, W.; Lee, S. Y.; Jung, Y. S.; Kim, S.-H.; Kim, H.-T., Flexible and Robust Superomniphobic Surfaces Created by Localized Photofluidization of Azopolymer Pillars. *ACS Nano* **2017**, *11* (8), 7821-7828.

76. Hensel, R.; Helbig, R.; Aland, S.; Braun, H.-G.; Voigt, A.; Neinhuis, C.; Werner, C., Wetting Resistance at Its Topographical Limit: The Benefit of Mushroom and Serif T Structures. *Langmuir* **2013**, *29* (4), 1100-1112.

77. Liu, T. L.; Kim, C.-J. C., Turning a surface superrepellent even to completely wetting liquids. *Science* **2014**, *346* (6213), 1096-1100.

78. Domingues, E. M.; Arunachalam, S.; Mishra, H., Doubly Reentrant Cavities Prevent Catastrophic

- Wetting Transitions on Intrinsically Wetting Surfaces. *ACS Applied Materials & Interfaces* **2017**, *9* (25), 21532-21538.
79. Yang, Y.; Li, X.; Zheng, X.; Chen, Z.; Zhou, Q.; Chen, Y., 3D-Printed Biomimetic Super-Hydrophobic Structure for Microdroplet Manipulation and Oil/Water Separation. *Adv Mater* **2018**, *30* (9).
80. Zheng, D.; Jiang, Y.; Yu, W.; Jiang, X.; Zhao, X.; Choi, C. H.; Sun, G., Salvinia-Effect-Inspired "Sticky" Superhydrophobic Surfaces by Meniscus-Confined Electrodeposition. *Langmuir* **2017**, *33* (47), 13640-13648.
81. Clemente, C. J.; Bullock, J. M. R.; Beale, A.; Federle, W., Evidence for self-cleaning in fluid-based smooth and hairy adhesive systems of insects. *The Journal of Experimental Biology* **2010**, *213* (4), 635-642.
82. Jiang, Y.; Liu, G.; Zhou, J., A novel process for circle-like 3D microstructures by two-step wet etching. *Journal of Micromechanics and Microengineering* **2009**, *19* (1).
83. Lei, K. F., Chapter 1. Materials and Fabrication Techniques for Nano- and Microfluidic Devices. In *Microfluidics in Detection Science*, 2014; pp 1-28.
84. Lei, K. F., Chapter 1 Materials and Fabrication Techniques for Nano- and Microfluidic Devices. In *Microfluidics in Detection Science: Lab-on-a-chip Technologies*, The Royal Society of Chemistry: 2015; pp 1-28.

Chapter 6. Acknowledgments

2년이라는 짧으면 짧고 길면 긴 시간동안 함께 지낸 실험실 사람들 모두 감사합니다. 처음 유니스트라는 학교를 와서 아무것도 모르는 채로 실험실 생활을 하게 되었는데, 모두 잘 도와줘서 재미있는 학교생활을 할 수 있었습니다. 아무것도 모르는 저를 대학원생으로 받아 주시고 많은 가르침을 주신 이동욱 교수님 항상 감사합니다. 교수님 덕분에 2년 동안 많은 것을 배울 수 있었고 좋은 경험을 얻을 수 있었습니다. 항상 감사합니다. 그리고 모르는 것이 있을 때마다 가르쳐 주셨던 백명진 박사님, 임찬웅 박사님 감사합니다. 박사님들 덕분에 많은 것을 배울 수 있었습니다. 그리고 랩장으로서 항상 나를 챙겨준 진태, 2년 동안 나를 잘 따라준 진우, 정준이 그리고 그 외에도 우리 실험실 사람들 모두 감사합니다.

학위논문심사를 도와 주신 곽상규 교수님, 서관용 교수님 바쁘신 와중에도 학위논문심사를 해주시고 더 나은 논문 작성을 위해 도와주셔서 감사합니다. 그리고 같이 논문을 진행하는 분들도 감사합니다. 덕분에 더 좋은 논문을 쓸 수 있었습니다. 학위논문심사를 위해 같이 알아보고 고생한 찬희 너무 고맙다.

그리고 제가 대학원 생활을 하게 해준 부모님 너무 고맙습니다. 2년이라는 시간 동안 저를 믿고 대학원 생활을 하게 해주시고 뒤에서 응원해 주셔서 감사합니다. 앞으로도 더 열심히 노력해서 좋은 곳에 취직하여 더 이상 걱정 안 하시게 노력하겠습니다. 그리고 대학원 생활하는 동안 많이 챙겨준 내 친구들 모두 너무 고맙다.